Charles University
Faculty of Science

Study programme: Physical Chemistry
Study branch: Physical Chemistry

Bc. Jaroslav Vacek

Theoretical Study of Influence of Silanol Nest Defects on Hydrolysis of Zeolite Chabazite

Teoretická studie vlivu defektů silanolového hnízda na hydrolýzu zeolitu chabazitu

MASTER THESIS

Supervisor of the master's thesis: RNDr. Lukáš Grajciar, Ph.D.
Department of Physical and Macromolecular Chemistry

Prague 2020

I declare that I carried out this master's thesis independently, and only with the cited sources, literature and other professional sources. It has not been used to obtain another or the same degree.

I understand that my work relates to the rights and obligations under the Act No. 121/2000 Sb., the Copyright Act, as amended, in particular the fact that the Charles University has the right to conclude a license agreement on the use of this work as a school work pursuant to Section 60 subsection 1 of the Copyright Act.

In .... date ....
Author's signature

Firstly, I would like to especially thank to my supervisor, RNDr. Lukáš Grajciar, Ph.D., for being so patient with me. I would like to thank for his systematic, effective and professional leadership. I would also like to thank to Christopher James Heard, Ph.D. for helping me and advising me on my research. I am also grateful to Mingxiu Liu, my coworker, as she has done some of the calculations in this thesis and was of a general help. My thanks go to prof. RNDr. Petr Nachtigall, PhD. and all members of his research group.

As well, I would like to thank to my family an my dearest, as they have been a great and constant support, practical, material but most importantly psychical support. Thank you for being here for me.

Title: Theoretical Study of Influence of Silanol Nest Defects on Hydrolysis of Zeolite Chabazite

Author: Bc. Jaroslav Vacek

Department: Department of Physical and Macromolecular Chemistry

Supervisor: RNDr. Lukáš Grajciar, Ph.D., Department of Physical and Macromolecular Chemistry

Abstract: This thesis is focused on theoretical study of influence of the silanol nest defects on the hydrolysis of zeolite Chabazite under harsh steaming conditions. The motivation of the thesis was a recent experiment proving that the silanol nest defect enhances the hydrolysis of a zeolite. The harsh steaming conditions have been chosen as some important technological processes involving zeolites require high temperatures and have water vapour present. The study was performed by using density functional theory calculations. To investigate the influence of the defect two models were used, a reference pristine model and a defected model containing the silanol nest defect. The two models were pure siliceous Chabazite periodical models with supercell containing 36 and 35 Si tetrahedra respectively. A multi-step hydrolysis leading to detachment of a $Si(OH)_4$ cluster from the zeolite, known as total desilication, was calculated for the two models. Multiple possible paths of the hydrolysis were discovered, compared and discussed on both models. Both the most favourable hydrolysis paths of the two model as well as their arithmetic means were compared. The experimentally set expectations that a silanol nest defect enhances the hydrolysis of the zeolite have been met.

Keywords: Density functional theory, Zeolites, Hydrolysis, Chabazite, Silanol nest

Název práce: Teoretická studie vlivu defektů silanolového hnízda na hydrolýzu zeolitu chabazitu

Autor: Bc. Jaroslav Vacek

Katedra: Katedra fyzikální a makromolekulární chemie

Školitel: RNDr. Lukáš Grajciar, Ph.D., Katedra fyzikální a makromolekulární chemie

Abstrakt: Tato práce je soustředěna na výzkum vlivu defektu silanolového hnízda na hydrolýzu zeolitů v přítomnosti horké vodní páry. Motivací této studie jsou nedávné experimentální práce, které ukazují, že přítomnost silanolového hnízda usnadňuje a urychluje hydrolýzu zeolitů. Přítomnost horké vodní páry simuluje podmínky podobné těm, které doprovází některé významné průmyslové procesy. Výzkum samotný byl proveden s využitím výpočtů pomocí teorie funkcionálu hustoty. K určení vlivu silanolového hnízda na hydrolýzu Chabazitu byly použity dva modely, nedefektní model s ideální jednotkovou celou a defektní model obsahující silanolové hnízdo. Oba modely byly periodické modely čistě křemičitého Chabazitu s 36, respektive 35 Si tetraedry. Na obou modelech byla uvažována vícekroková hydrolýza vedoucí až k odělení klastru $Si(OH)_4$ od struktury zeolitu. Tento proces je znám jako totální desilikace. Na obou modelech bylo nalezeno více možných cest hydrolýzy, které byly porovnány a diskutovány. Výsledky z obou modelů pak byly porovnány navzájem a to jak nejpříznivější cesty hydrolýzy z obou modelů, tak aritmetické průměry všech uvažovaných cest. Získaná data naplnila očekávání stanovená experimentem, že silanolové hnízdo usnadňuje

a urychluje hydrolýzu zeolitu.

Klíčová slova: Teorie funkcionálu hustoty, Zeolity, Hydrolýza, CHA, Silanolové hnízdo

List of Abbreviations

FCC - Fluid Catalytic Cracking
DFT - Density Functional Theory
LDA - Local Density Approximation
GGA - General Gradient Approximation
PBE - functional by Perdew, Burke and Erzenhof
vdW - van der Waals force
NMR - Nuclear Magnetic Resonance
PES - Potential Energy Surface
R - Reactant
P - Product
TS - Transitional State
NEB - Nudged Elastic Band method
cNEB - Climbing Image Nudged Elastic Band
CHA - Chabazite
MFI - A zeolite structure VASP - Vienna Ab initio Simulation Package
VTST - VASP Transition State Tools
PWA - Projector Augmented Wave
IP - Intermediate Product
I - Inverted path
NI - Non-Inverted path
P - Pristine
D - Defected
MD - Molecular Dynamics

Contents

Introduction

Zeolites are a group of microporous crystalline aluminosilicates. The structure of zeolites consists of corner-sharing silicate and alumina tetrahedra. The central atom of the tetrahedra is known as a T-atom. Other so-called heteroatom can be present, such as Gallium, Tin and Germanium. Zeolitic framework is cross-linked with a network of canals of well-defined sizes which greatly enlarges the active surface of the zeolites. This gives zeolites, in general, a broad catalytic potential. Zeolites are commonly used as heterogeneous catalysts in many industrial processes, namely oil cracking. [1] [2]

Some of the catalytic processes involving zeolites, like fluid catalytic cracking (FCC), are inherently connected with the presents of hot water vapour. Zeolites are known to degrade under such conditions via hydrolysis. The catalyst loses it catalytic properties over time. Therefore, zeolite hydrolysis had been and is being extensively researched both theoretically and experimentally. The goal is the understanding of the mechanism, not only for academic interest but with prospect of potential future catalysts improvements. [3] [4][5]

A known and experimentally documented defect occurring in the zeolites structure is called silanol nest. This defect occurs when a single T-atom is not present in the framework, and the associated oxygen atoms are caped with a hydrogen atom. The four OH groups forming the silanol nest react with each other via hydrogen bonds, thus greatly stabilising the structure. The effects of defects on the zeolite hydrolysis mechanism are yet not completely understood. Some of the recent experimental work suggests that they may play a key role. The goal of this thesis is to find the mechanism of the hydrolysis, identify rate determining step and compare the pristine zeolite with a defected structure.[6] [7]

1. Computational Chemistry

In the past thirty years, computational chemistry has become a well established field of scientific research. Not only can it correspond well with experiment computational chemistry is capable of providing information, which is experimentally unobtainable. In this thesis, only the static methods of quantum chemistry were used with no temperature correction. Namely the density functional theory (DFT) has been used.

1.1 Density Functional Theory (DFT)

Traditional *ab initio* methods of quantum chemistry (such as post-Hartree-Fock methods) solve Schrödinger's equation by determining the wave function Ψ. The wave function is a $4N$ (or $3N$ for closed shell systems) dimensional function, where N stands for the number of electrons of the system. Therefore, from calculation point of view, it is uneasy, to determine or operate with Ψ. Density Functional Theory is an alternative approach of quantum chemistry.

The electron density ρ is a function of the three spatial coordinates, as it describes only the spatial distribution of electrons. This makes it much easier to determine and calculate with in comparison with the wave function. Methods of DFT are capable of dealing with large (and periodical) systems, while having reasonable accuracy.

DFT is based on the two Hohenberg-Kohn theorems. First of the Hohenberg-Kohn theorems states that all ground-state properties of a system are given solely by electron density of the system. The electronic energy E_{el} is a functional of electron density $\rho(\overrightarrow{r})$:

$$E_{el} = E[\rho(\overrightarrow{r})]. \tag{1.1}$$

The second theorem proves that calculations performed with the electron density of the system can give only greater or equal energy to the real energy of the system. The second theorem mirrors the variation principle in the traditional quantum mechanics. However, second theorem is valid only for an exact functional of energy, which is in practise unobtainable.[8][9] [10]

The two Hohenberg-Kohn theorems are a theoretical base of DFT, they however, do not indicate the form of the functional $E[\rho(\overrightarrow{r})]$. A practical way to calculate the DFT based problems are Kohn-Sham equations.[11]. This approach is inspired by the Hartree-Fock method. The Kohn-Sham equations have general form.

$$\hat{f}^{KS}\phi_{KS,i} = \varepsilon_i\phi_{KS,i}, \tag{1.2}$$

where $\hat{f}^{KS}$ is the Kohn-Sham operator, $\phi_{KS,i}$ is an one-electron wave function and ε_i is the eigenvalue of the operator $\hat{f}^{KS}$ for the given function, the energy. The Kohn-Sham operator $\hat{f}^{KS}$ is an one-electron operator which can be expressed:

$$\hat{f}^{KS} = -\frac{1}{2}\nabla^2 + V_S(\overrightarrow{r}), \tag{1.3}$$

where ∇^2 is the operator of kinetic energy (in arbitrary units), and $V_S(\overrightarrow{r})$ is the local effective potential, a local potential within the model of independent-electrons. In order to calculate the Kohn-Sham equations a set of orbital-like one-electron wave functions must be provided, $\phi_{KS,i}$. The $\phi_{KS,i}$ wave functions, known as Kohn-Sham orbitals, correspond to the density $\rho(\overrightarrow{r})$:

$$\rho(\overrightarrow{r}) = \sum_i |\phi_{KS,i}|^2. \tag{1.4}$$

The physical meaning of Kohn-Sham orbitals used to be dismissed. Lately, they are viewed by some as the best representation of the system within the independent electron approximation. [12] Kohn-Sham equations can be solved iteratively, starting with a trial $\phi_{KS,i}$. Then the equations 1.2 are solved and a new $\phi_{KS,i}$ obtained. This cycle continues until self-consistency is reached, like with Hartree-Fock equations. [13]

The energy functional $E[\rho(\overrightarrow{r})]$ can be expressed:

$$E[\rho(\overrightarrow{r})] = T_e[\rho(\overrightarrow{r})] + V_{Ne}[\rho(\overrightarrow{r})] + V_{ee}[\rho(\overrightarrow{r})] + E_{XC}[\rho(\overrightarrow{r})], \tag{1.5}$$

where $T_e[\rho(\overrightarrow{r})]$ is the functional of kinetic energy of non-interacting electrons, $V_{Ne}[\rho(\overrightarrow{r})]$ is the functional of interaction of electrons and nuclei, $V_{ee}[\rho(\overrightarrow{r})]$ is the functional of electron-electron interaction (repulsion) and $E_{XC}[\rho(\overrightarrow{r})]$ is the functional of the exchange and correlation energy. From the Kohn-Sham equations the $E[\rho(\overrightarrow{r})]$ can be expressed:

$$\begin{aligned} E[\rho(\overrightarrow{r})] = &- \frac{1}{2}\sum_i \langle \phi_{KS,i}|\nabla^2|\phi_{KS,i}\rangle + \sum_{nuclei,A} Z_A \int \frac{\rho(\overrightarrow{r}_1)}{(\overrightarrow{r}_{1,A})} d(r_1) \\ &- \frac{1}{2}\iint \frac{\rho(\overrightarrow{r}_1)\rho(\overrightarrow{r}_2)}{(\overrightarrow{r}_{1,2})} d(r_1)d(r_2) + E_{XC}[\rho(\overrightarrow{r})], \end{aligned} \tag{1.6}$$

where Z_A is a charge of a nuclei A. All the above mentioned functionals (1.6) can be easily worked with, except the last functional. The functional of exchange and correlation energy is troublesome, as its exact form is unknown.

One of the main goals in DFT-based research is to find an accurate form of the functional of the exchange and correlation energy. DFT calculation, however, perform reasonable well even with very simple and computationally efficient approximated functionals. A number of approximate forms of the functional of the exchange and correlation energy have been derived from the model of homogeneous electron gas, an idealised model of homogeneous electron distribution throughout the space. Even though this is a simple and somewhat non-realistic model, it can provide a very good approximative form of the $E_{XC}[\rho(\overrightarrow{r})]$. It should be noted that other approximated functionals of the exchange and correlation energy have been derived, from other model systems.

The most basic approximation is known as the Local Density Approximation (LDA). On LDA level of theory, the exchange and correlation energy in any given point depends only on the value of the $\rho(\overrightarrow{r})$ in that given point: [14]

$$E_{XC}^{LDA}[\rho(\overrightarrow{r})] = \int \rho(\overrightarrow{r})[e_x(\rho(\overrightarrow{r})) + e_c(\rho(\overrightarrow{r}))]dr, \tag{1.7}$$

where e_x and e_c are the exchange and correlation energies per electron, as derived from the model of unpolarized homogeneous electron gas. [8]

An improvement over LDA is the General Gradient Approximation (GGA) which is also a local approximation. Within the GGA level of theory, the exchange and correlation energy in a given point depends on the value of the $\rho(\overrightarrow{r})$ and on its gradient $\nabla(\rho(\overrightarrow{r}))$ in that given point:

$$E_{XC}^{GGA}[\rho(\overrightarrow{r})] = \int \rho(\overrightarrow{r}) f[(\rho(\overrightarrow{r})), \nabla(\rho(\overrightarrow{r}))]dr. \tag{1.8}$$

GGA based functionals perform much better than LDA, while being only slightly more computationally demanding. A GGA level functional by Perdew, Burke and Erzenhof (PBE) has been used in this thesis. [13] [15][14][16]

The local character of PBE and all local functionals makes them incapable of a good representation of long-rage interactions, such as van der Waals's forces. The dispersion forces are, however, essential for reactions within zeolitic channels. Functionals on higher level of theory (vdW functional) are capable of capturing dispersion interactions. However, such calculations would be too costly for a study of a periodic system of the size of a model used in thesis, with questionable consistency. Therefore, a semiempirical forcefield-based D3 dispersion correction by Grimme was used, with damping by Becke and Johnson. The semiempirical dispersion correction is a rather consistent and reliable way of representing the dispersion interactions, while it adds very little to the overall calculation demand. [17][18]

1.2 Periodic Boundaries Condition Model

To perform a study of solid state crystalline material, a suitable model must be used. A Periodic Boundaries Condition Model is a very good representation of macro-size crystalline material. The main idea of this model is to define an unit cell of the studied material and then expand it to infinity in all directions.

The basic principles have been established by Felix Bloch in the 1920s. Bloch used the model of independent electrons and introduced an *effective potential* $V(\overrightarrow{r})$. As mentioned above, the $V(\overrightarrow{r})$ reduces the problem to a single electron problem, greatly reducing the complexity of the problem.

Bloch has theorized that the $V(\overrightarrow{r})$ has a periodical character following the periodicity of the model. First Bloch defined the primitive lattice translation vector $\overrightarrow{T}$:

$$\overrightarrow{T} = n_1\overrightarrow{a_1} + n_2\overrightarrow{a_2} + n_3\overrightarrow{a_3}, \tag{1.9}$$

where $\overrightarrow{a_1}, \overrightarrow{a_2}, \overrightarrow{a_3}$ are the lattice vectors, and $n_1, n_2, n_3 \in \mathbb{N}$. The potential follows the same periodicity as the system:

$$V(\overrightarrow{r} + \overrightarrow{T}) = V(\overrightarrow{r}). \tag{1.10}$$

All periodical functions can be expanded to a Fourier series, so the potential can be expressed:

$$V(\overrightarrow{r}) = \sum_{\overrightarrow{K}} V_{\overrightarrow{K}} e^{i\overrightarrow{K}\overrightarrow{r}}, \tag{1.11}$$

where $\overrightarrow{K}$ are vectors of reciprocal space to the direct space determined by equation 1.9 and the $V_{\overrightarrow{K}}$ is expressed:

$$V_{\overrightarrow{K}} = \frac{1}{\sqrt{\Omega}} \int V(\overrightarrow{r}) e^{-i\overrightarrow{K}.\overrightarrow{r}} dr, \tag{1.12}$$

where Ω is the volume of a reciprocal unit cell.

Bloch's theorem states that the wavefunction in periodic conditions can be expressed as Bloch periodic wavefunction $\Psi_{\overrightarrow{k}}(\overrightarrow{r})$: [19][16]

$$\Psi_{\overrightarrow{k}}(\overrightarrow{r}) = e^{i\overrightarrow{k}\overrightarrow{r}} u_{\overrightarrow{k}}(\overrightarrow{r}), \tag{1.13}$$

where $u_{\overrightarrow{k}}(\overrightarrow{r})$ is periodic function with same periodicity as Bravais lattice, $\overrightarrow{k}$ is the wavevector, so $e^{i\overrightarrow{k}.\overrightarrow{r}}$ can be seen as plane waves.

As $u_{\overrightarrow{k}}(\overrightarrow{r})$ is a periodic function it can be expanded to a Fourier series much like equations 1.11 and 1.12. By applying this to equation 1.13 we get:

$$\Psi_{\overrightarrow{k}}(\overrightarrow{r}) = e^{i\overrightarrow{k}\overrightarrow{r}} \frac{1}{\sqrt{\Omega}} \sum_{\overrightarrow{K}} u_{\overrightarrow{k}}(\overrightarrow{K}) e^{i\overrightarrow{K}\overrightarrow{r}}, \tag{1.14}$$

where $u_{\overrightarrow{k}}(\overrightarrow{K})$ are the Fourier coefficients.

In order to use Bloch periodic wavefunction for calculations it must be expanded to a basis of a finite number of members. Plane waves $\phi^{\overrightarrow{k}}_{\overrightarrow{K}}$ can be used as the basis set:

$$\phi^{\overrightarrow{k}}_{\overrightarrow{K}} = \frac{1}{\sqrt{\Omega}} e^{i(\overrightarrow{k}+\overrightarrow{K})\overrightarrow{r}}. \tag{1.15}$$

The higher members of the series 1.15 have a higher energy. The number of members of the series 1.15 is a parameter of the calculation known as the kinetic energy cut-off. Adding energetically higher plane waves increases the accuracy but makes the calculations more demanding. In practice the cut-off value must be set at cost-effective level.

In the reciprocal space, the Brillouin zone is an unique representation of a primitive cell. The electron density $\rho(\overrightarrow{r})$, as all other properties of the periodical model, can be expressed within the 1th Brillouin zone as an integral:

$$\rho(\overrightarrow{r}) = \frac{1}{\Omega} \sum_{n} \int_{BZ} f_{n\overrightarrow{k}} |\psi_{n\overrightarrow{k}}|^2 dk, \tag{1.16}$$

where $\overrightarrow{k}$ is the Bloch vector, n is the band index and $f_{n\overrightarrow{k}}$ is the occupational number (for the given Bloch vector and band index). The band index n is of a similar order as the number of electrons per unit cell. There is, however, an infinite number of Bloch vectors in each unit cell, making integral 1.16 basically intractable. However, the wavefunctions for a similar Bloch vector $\overrightarrow{k}$ are also very similar. So the $\rho(\overrightarrow{r})$ can be approximately expressed as a sum:

$$\rho(\overrightarrow{r}) = \sum_{n,\overrightarrow{k}} \omega_k f_{n\overrightarrow{k}} |\psi_{n\overrightarrow{k}}|^2, \tag{1.17}$$

where $\omega_k f_{n\overrightarrow{k}}$ is the transformed occupational number $f_{n\overrightarrow{k}}$.

This in terms mean we can sample the wavefunctions only for some Bloch vectors $\overrightarrow{k}$, for some so-called k-points. We have reduced the infinite number of Bloch vectors to a set of discrete points within the 1th Brillouin zone. The k-point sampling is a parameter of the calculation. A large unit cell corresponds to a small reciprocal Brillouin cell. The k-point sampling needs to be more dense for small unit cell in real space then for large ones. [20]

Most chemical properties are given by the valence electron shell. Therefore, a frozen-core approximation is often implied. The core electrons are not represented by a proper wavefunction but by a pseudopotential. A pseudopotential represents the shielding of the nuclear charge by the inner electron shells. It had to be determined for each atom just once and it is very cost-effective. The frozen-core approximation makes large periodic calculations possible. On the down side, pseudopotentials are not capable of any correlation interactions with the valence electron shell, which would lead to further stabilisation. Pseudopotentials as well are not capable of a precise description of the magnetic shielding constants, necessary for precise NMR calculations.[21]

1.3 Potential Energy Surface (PES)

The potential energy surface (PES) is the cornerstone concept of computational chemistry. The PES is a function of energy of a system (molecule or a crystal) in respect to the position of every nuclei of every atom. PES thus gives us an energy of the system for any given geometry. As position of a nuclei is determined by three coordinates. PES is general (for nonlinear systems) $3N$-6 dimensional, where N stands for the number of atoms. This in terms means that even for small molecules PES becomes a complicated multidimensional function. To calculate a complete PES of a system is extremely computationally demanding, in fact it is possible to calculate a complete PES only for a very small systems. Moreover, larger parts of the PES are not interesting from a chemical point of view. The PES is thus studied locally, and only for relevant structures. [22]

Studying the PES is focused on finding stationary points. Stationary point $\overrightarrow{a}$ of multidimensional function f is defined by having its gradient equal to zero:

$$\overrightarrow{\nabla} f(\overrightarrow{a}) = \overrightarrow{0}. \tag{1.18}$$

Stationary points fall in three categories: maximum, minimum and saddle points. A chemical reaction can be described as the shift of a system from one minimum (a reactant-R) to other minimum (a product-P) while overcoming a saddle point of the first order (transitional state- TS). Locating this stationary points is the key to understanding the reaction mechanism. A path on the PES that passes through a saddle point of the first order is reaction coordinate. That being said, the two minimums can be connected by multiple saddle points. To determine a minimum or a TS a Hessian matrix of second derivatives is used (we differentiate the PES according to coordinates of atoms). A minimum will have all Hessian matrix eigenvalues positive, meanwhile a TS will have one and only one matrix eigenvalue negative. Eigenvalues of Hess's matrix correspond to vibration modes (within the harmonic oscillator approximation). Therefore, the TS have a single imaginary vibration mode frequency and that vibration mode dictates the direction of the reaction.[23][24]

1.4 Methods of Localisation of TS

Two groups of TS locating method have been used in this thesis, the global method (like NEB) and the local method (like dimer). The global method approaches to finding the TS by mapping the PES in multiple positions. The local methods rely on locating the TS from one guess structure, provided the guess structure is close enough to the TS. The global methods used in this thesis will be discussed first.

An important tool for locating TS on a PES is the Nudged Elastic Band method (NEB). NEB is an iteration on older methods of the same principle, like the Chain-of-states method. The core idea of NEB is to map the PES by a number of so-called images, structures placed along the reaction coordinate, from reactant to product. A stable structure, a local minimum, needs to be placed on both ends of the string of images, a reactant and a product. The string of images is then optimised.

If the images would be simply optimised they would just converge to respective minimum. An artificial force needs to stop them from falling down to the minimum. Thus an artificial spring force is introduced. A force acting on an image i within Chain-of-states method the can be expressed:

$$\overrightarrow{F_i} = -\overrightarrow{\nabla} V(\overrightarrow{R_i}) + \overrightarrow{F_i^s}, \tag{1.19}$$

where the $-\overrightarrow{\nabla} V(\overrightarrow{R_i})$ is the real potential force and the $\overrightarrow{F_i^s}$ is the spring force. A simple spring force with a set spring constant k have been tested in the early days of the method, which can be expressed:

$$\overrightarrow{F_i^s} \equiv k_{i+1}(\overrightarrow{R}_{i+1} - \overrightarrow{R_i}) - k_i(\overrightarrow{R_i} - \overrightarrow{R}_{i-1}). \tag{1.20}$$

This simple spring force works to some extend, it however, suffers from two main problems. Firstly, the component off the spring force that is perpendicular to the path (and thus is perpendicular to the $\overrightarrow{\nabla} V(\overrightarrow{R_i})$) tends to pull the chain of images of the reaction coordinate (phenomena known as corner-cutting). Secondly, the real potential force $-\overrightarrow{\nabla} V(\overrightarrow{R_i})$ is larger near the TS. The component of spring force that is parallel to the path (and thus is parallel to the $\overrightarrow{\nabla} V(\overrightarrow{R_i})$) can compensate for this only by increasing the distance between the images near TS. This leads to uneven spacing between the images. Larger distance between the images near TS means that the sampling in the proximity of the TS is scarce. The proximity of the TS is, however, the most important part of the PES to be sampled.

A more complex projection of the spring force had to be implemented. The total force within the NEB method exerted on an image i can be expressed:

$$\overrightarrow{F}_i^{NEB} = -\overrightarrow{\nabla} V(\overrightarrow{R_i})_\perp + \overrightarrow{F_i^s}_\parallel. \tag{1.21}$$

The perpendicular component $\overrightarrow{\nabla} V(\overrightarrow{R_i})_\perp$ can be expressed:

$$\overrightarrow{\nabla} V(\overrightarrow{R_i})_\perp = \overrightarrow{\nabla} V(\overrightarrow{R_i}) - \overrightarrow{\nabla} V(\overrightarrow{R_i}) \cdot \overrightarrow{\tau}_i \overrightarrow{\tau}_i, \tag{1.22}$$

where $\overrightarrow{\tau}_i$ is an unit tangent to the path (the reaction coordinate on the PES) for the image i. In a similar fashion the parallel component of the spring force $\overrightarrow{F_i^s}_\parallel$ can be expressed:

$$\overrightarrow{F_i^s}_\parallel = \overrightarrow{F_i^s} \cdot \overrightarrow{\tau}_i \overrightarrow{\tau}_i. \tag{1.23}$$

This projection of the perpendicular component of the $\overrightarrow{\nabla} V(\overrightarrow{R_i})$ and the parallel component of the spring force (as seen in equation 1.21) is know as "nudging". This projection of the forces doesn't interfere with optimization (relaxation) of the images, the optimized image fulfils the condition $\overrightarrow{\nabla} V(\overrightarrow{R_i})_\perp = 0$, if the image lies on the reaction coordinate. The nudged projection of the force maintains even spacing of the images. The method performance does not depend on the real value of k. [25]

The NEB method samples the reaction coordinate by a number of structures. The structure with the highest energy, however, doesn't have to be the TS. An improved method is known as Climbing Image Nudged Elastic Band method (cNEB). The cNEB method is only slightly different from the regular NEB. The calculation runs for few steps as regular NEB, then the image with the highest energy i_{max} is recognised. This image is then subjected to a different force then the rest of the images (as seen in equation 1.21):

$$\overrightarrow{F}_{i_{max}} = -\overrightarrow{\nabla} V(\overrightarrow{R}_{i_{max}}) + 2\overrightarrow{\nabla} V(\overrightarrow{R}_{i_{max}}) \cdot \overrightarrow{\tau}_{i_{max}} \overrightarrow{\tau}_{i_{max}}. \tag{1.24}$$

It is the full potential force $\overrightarrow{F}_{i_{max}}$ with the component parallel to the path inverted. The i_{max} is not subjected to the spring force at all. The $\overrightarrow{F}_{i_{max}}$ will push the image parallel to the path towards the saddle point, reaching the structure of the TS. The cNEB method is not much more computationally demanding than the NEB. It can, however, provide the structure of the real TS. On the other hand, simple NEB is a more robust tool.[26]

A second method of finding TS is known as dimer method. The method involves setting up two structures, known as the "dimer". The structures, in general, have a very similar geometry, but they are offset from each other by a certain distance. The idea being that the TS is a structure between the two dimer structures.

The two dimer structures at $\overrightarrow{R_1}$ and at $\overrightarrow{R_2}$ are separated by the distance $2\Delta R$ with a point $\overrightarrow{R}$ in the middle. A defining factor of the dimer is the unity vector $\overrightarrow{N}$, known also as dimer axis, which connects structures $\overrightarrow{R_1}$ and $\overrightarrow{R_2}$. In practise, a guess structure at $\overrightarrow{R}$ must be provided. Vector $\overrightarrow{N}$ is than estimated, usually by performing a vibration analysis of the guess structure. The imaginary mode with the highest frequency is usually used. The dimer is then set around the guess structure at $\overrightarrow{R}$ like this:

$$\begin{aligned} \overrightarrow{R_1} &= \overrightarrow{R} + \Delta R \overrightarrow{N} \\ \overrightarrow{R_2} &= \overrightarrow{R} - \Delta R \overrightarrow{N}. \end{aligned} \tag{1.25}$$

The energy of the dimer E is given as a simple sum of the energies of $\overrightarrow{R_1}$ and $\overrightarrow{R_2}$: $E = E_1 + E_2$. The energy of the middle point E_0 and the force exerted on the middle point $\overrightarrow{F_R}$ are calculated in relation to the dimer structures $\overrightarrow{R_1}$ and $\overrightarrow{R_2}$. The force $\overrightarrow{F_R}$ is a simple average of forces $\overrightarrow{F_1}$ and $\overrightarrow{F_2}$ exerted on $\overrightarrow{R_1}$ and $\overrightarrow{R_2}$: $\overrightarrow{F_R} = \frac{1}{2}(\overrightarrow{F_1} + \overrightarrow{F_2})$. The energy E_0 is derived from the finite difference formula for the curvature of the potential C along the dimer:

$$C = \frac{(\overrightarrow{F_1} - \overrightarrow{F_2})\overrightarrow{N}}{2\Delta R} = \frac{E - 2E_0}{(\Delta R)^2}. \tag{1.26}$$

The energy E_0 is given by this relation:

$$E_0 = \frac{E}{2} + \frac{\Delta R}{4}(\overrightarrow{F_1} - \overrightarrow{F_2})\overrightarrow{N}. \tag{1.27}$$

All the properties of the dimer are given only by calculating $\overrightarrow{R_1}$ and $\overrightarrow{R_2}$. This makes for effective calculations and easy parallelization of the computation.

Every step of optimization of the dimer starts with a single step rotation. The two dimer structures rotated around the middle point $\overrightarrow{R}$ which is stationary. The energy, E_0, is constant throughout the rotations. Since the distance ΔR is also constant the only thing that changes is the energy of the dimer E and the mode of curvature C. As seen in equation 1.26 the minimum energy E corresponds with the smallest possible curvature.

The force of rotation is defined as $\overrightarrow{F}^{\perp} = \overrightarrow{F_1}^{\perp} - \overrightarrow{F_2}^{\perp}$, where $\overrightarrow{F_i}^{\perp} \equiv \overrightarrow{F_i} - (\overrightarrow{F_i} \cdot \overrightarrow{N})\overrightarrow{N}$ for $i = 1, 2$. The rotation force together with $\overrightarrow{N}$ define the plane of rotation with unit vector $\overrightarrow{\Theta}$. The energy is optimized in respect to angle θ, the angle representing the rotation of $\overrightarrow{\Theta}$ in the space.

The second step of dimer optimization is translation. The real potential force $-\overrightarrow{\nabla}V(\overrightarrow{R})$ would move the dimer to the nearest minimum. A special force $\overrightarrow{F}^{\dagger}$ has to be defined:

$$\overrightarrow{F}^{\dagger} = -\overrightarrow{\nabla}V(\overrightarrow{R}) + 2\overrightarrow{\nabla}V(\overrightarrow{R})_{\parallel}, \tag{1.28}$$

where the $-\overrightarrow{\nabla}V(\overrightarrow{R})_{\parallel}$ is the component of the real potential force $-\overrightarrow{\nabla}V(\overrightarrow{R})$ parallel with the vector $\overrightarrow{N}$. The vector $\overrightarrow{N}$ has oriented itself to cover the smallest curvature C on the PES. By inverting the parallel component of the real potential force we get a final force $\overrightarrow{F}^{\dagger}$ directing towards the nearest saddle point. The dimer is then moved by a set distance on the PES in direction of the $\overrightarrow{F}^{\dagger}$. After this translation the dimer rotates again. The cycle of rotation and translation continues until a TS is reached. [27]

The dimer method is in general faster and more effective then the NEB/cNEB method. The dimer has to calculate only two structures per step, while NEB usually need at least three images to work. A larger number of images is usually used, most calculation in this thesis were done with six images. However, dimer is capable of finding only the nearest TS, as described above. The initial guess structure has to be generally very close to the actual TS. NEB/cNEB is much more robust tool as it samples more of the PES. The two methods work best in tandem: the reaction coordinate is first mapped using NEB. The image of the NEB with the highest energy can then be used as a guess structure for dimer. This approach utilises both the good coverage offered by NEB and the fast convergence of the dimer, if the TS is close.

2. Methodology

2.1 Models

Hydrolysis of zeolites leads to a T-O bond breaking. Each attacking water molecule breaks a single framework bond, while forming two OH groups. A complete detachment of a T-atom is, therefore, possible via a cascade of hydrolysis steps. This in term leads to a formation of a (new) silanol nest and a presence of extra-framework specie within the zeolitic channels. This process is known as a total desilication or dealumination (depending on the T-atom).

A Q-number of a T-atom refers to the number of oxygens bonding the T-atom to the framework of the zeolite. As mentioned above, standard T-atom in a zeolite structure occupies a tetrahedron with four oxygens in the tops, while each of the oxygens is connected to other T-atoms. Therefore, a standard T-atom in a zeolite structure is a Q^4 atom. The Q-number of a T-atom can be lower. The T-atom surrounding a silanol nest are only Q^3 atoms. As the hydrolysis proceeds and the atom becomes disconnected from the framework, its Q-number drops. A completely detached T-atom is a Q^0 atom.

Zeolite Chabazite (CHA) has been selected to be studied in this thesis. CHA type zeolites are commonly used in the industry, thus it is a good representation of real-live catalyst. From the calculation point of view, it offers many benefits. Firstly, CHA crystalline structure is highly symmetric, all T-atoms are equal. Therefore, any atom is a complete sample of the framework. Secondly, CHA has a small unit cell in comparison with other zeolite framework (for example MFI). This makes CHA a good model for fast and effective calculations.

Every T-atom in CHA is surrounded by four crystallographically distinguishable oxygens. The four crystallographically distinguishable oxygens are commonly numbered as can be seen in Figure 2.1. [28]

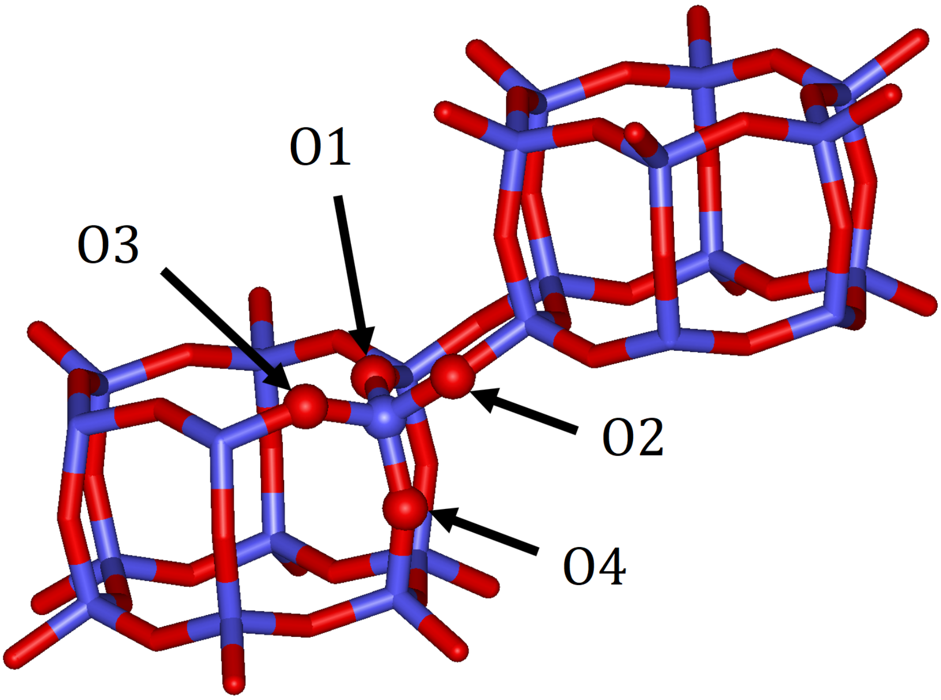

Figure 2.1: A cut-out of a CHA unit cell with a Si (T) atom marked. The crystallographically distinguishable oxygens are marked and numbered.

All calculations were performed on a periodical model of pure siliceous CHA. Essentially 2 models were used, in order to compare the effects of silanol nest to a reference system. First, model was a pristine (i.e. defectless) CHA. The structure have been downloaded from Database of Zeolite Structures as an experimentally obtained geometry [29]. Then the structure and the unit cell have been optimized. The second model was formed from pristine CHA by removing a single Si atom and adding hydrogen in the place of severed O-Si bonds. The structure was optimized but no changes to the unit cell have been made. The unit cell of both models had the volume of 2359.7035 $Å^3$. The unit cell vectors were a = 13.76457 Å, b = 13.81372 Å and c = 14.29992 Å. The unit cell angles were $\alpha = 90.0532°$, $\beta = 89.8817°$ and $\gamma = 119.7887°$. The unit cell of pristine CHA has the summary formula of $Si_{36}O_{72}$ and the unit cell of defected CHA has the summary formula of $Si_{35}O_{72}H_4$. The number of atoms in unit cell, however, varied as additional water molecules had to be added.

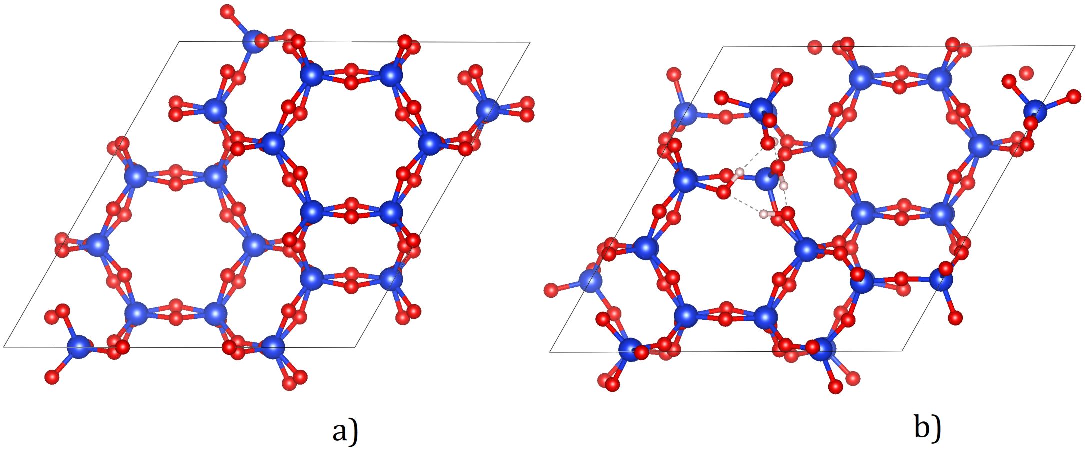

Figure 2.2: Unit cells of the two models used in this thesis: a) Pristine CHA, b) Defected CHA with a silanol nest.

2.2 Calculation details

All calculations were performed with VASP (Vienna Ab initio Simulation Package). [30] [31] The VASP-5.3.5 version of the code was used. A VTST code enhancement was used for all NEB and cNeb calculations. [27] [26].

The PBE functional was used which is on a GGA level of theory. [15]. An empirical dispersion by Grimme with Becke-Johnson damping was used.[17] [18] The k-point Γ sampling of the reciprocal space was used as it is sufficient for an unit cell of this volume. The kinetic energy cut-off was set to 400 eV, which has proven to be reliable for zeolite-like systems. The Periodic Projector Augmented Wave (PWA) have been used.

2.3 The Ways of Reporting Energy

Three main types of energies are being reported in this thesis, as can be seen in Figure 2.3, in a schematic depiction of using a dependence of energy on reaction coordinate.

The Figure 2.3 is a depiction of a schematic CHA hydrolysis reaction coordinate. First a water molecule is adsorbed within the CHA canal in a most stable, thus thermodynamically most probable, position **(R-T)**. The most stable local minimum doesn't have to be the best starting position for the reaction. Water molecule can be rearranged into a different less stable local minimum **(R-K)** while overcoming a transitional state **(ts)**. This **R-K** minimum is less stable, but it is a much better starting position for the reaction, representing the initial position of the most demanding step of the hydrolysis mechanism.

The **ts** isn't always present and can be difficult to be calculated. Energetic barrier of a water rearrangement or rotation is generally very small. This can be illustrated by water rearrangement in CHA channel in Figure 2.4.

As can bee seen in Figure 2.4, the E_{Act} is almost equal to E_{React}. Thus in this thesis **ts** connected with molecular rearrangement were neglected as too low to be important.

The reaction proceeds to form a high lying TS, which corresponds with covalent bond breaking and is the main barrier for the reaction. The reaction ends with a stable product **(P)**. In this thesis three energies are presented. First is the activation energy, E_{Act}. As can be seen in the Figure 2.3, it is the energy difference between the TS and the **R-K**. Second is the energy of the overall barrier E_{Bar}, which is the

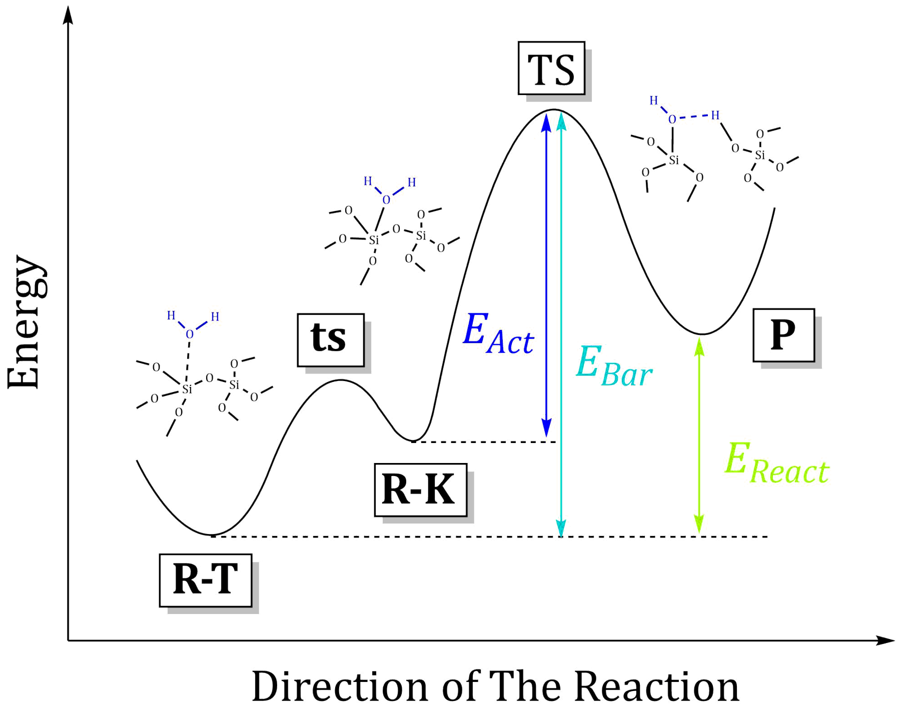

Figure 2.3: A schematic depiction of a CHA hydrolysis reaction coordinate.

difference between the TS and the **R-T**. Lastly, the reactional energy E_{React}, which is the difference between the **R-T** and the **P**.

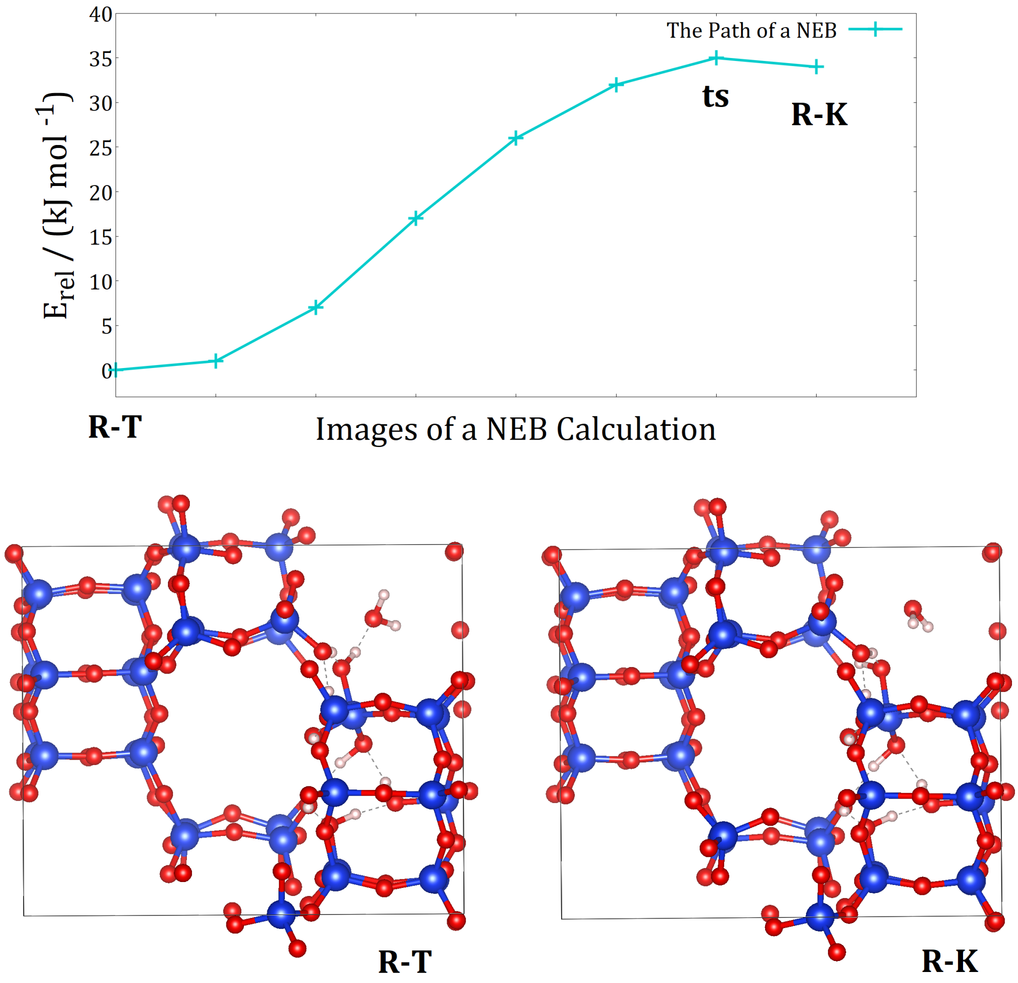

Figure 2.4: An example of a water molecule rotating from the optimal position **(R-T)** to a less stable position **(R-K)**. The **(R-K)** represents the initial position of the most demanding step of the hydrolysis mechanism. The rearrangement overcomes a small barrier **(ts)**. This example has been performed on the O3-O1-O2-O4 reactant (see Section 3.3.3).

3. Results

3.1 Pristine CHA

3.1.1 First Step (Q^4 to Q^3)

As all T-sites in CHA are symmetrically equivalent, any T-atom could be chosen. Four crystallographically distinguishable paths were proposed, each for one of the four crystallographically distinguishable oxygens (see Figure 2.1). A two step mechanism was discovered :

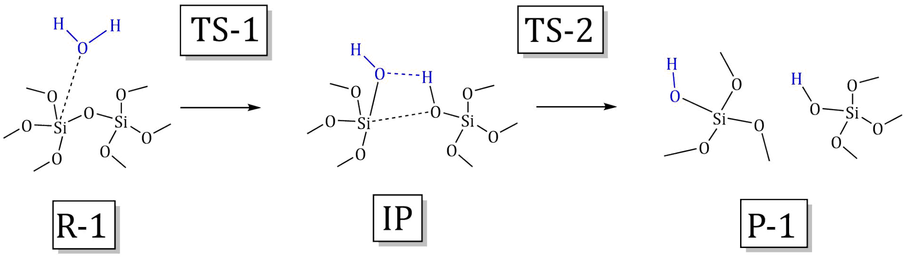

Figure 3.1: The mechanism of the first step of hydrolysis of the pristine CHA starts with a water molecule adsorbed in the CHA channel. Through the first transitional state (TS-1) an intermediate product (IP) is formed. This intermediate product, also known as equatorial product, can undergo a rotation accompanied inversion of the Si tetrahedron via second TS (TS-2) into a more stable final product (P-1), which is also known as axial product. The equatorial and axial notation has been established in relevant literature. [32]

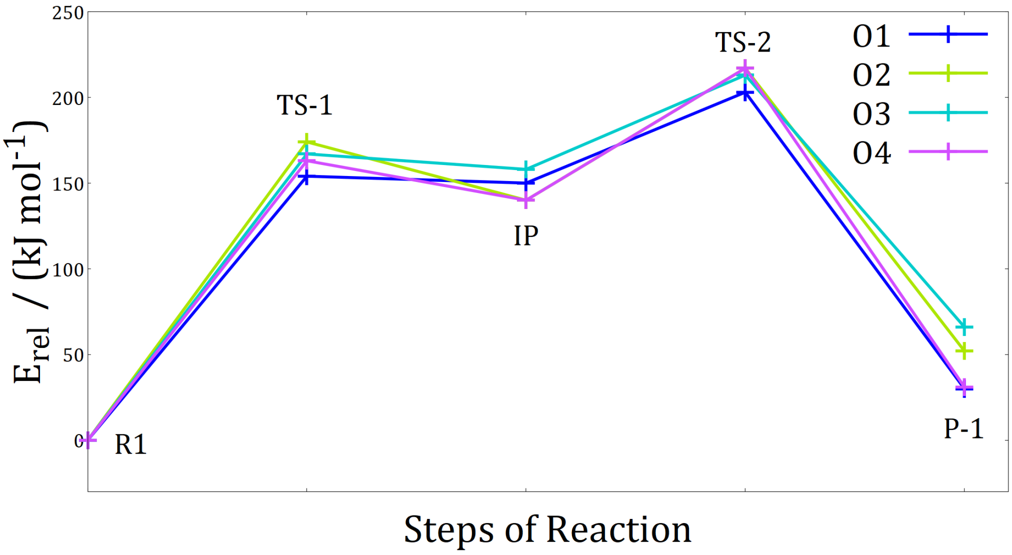

Figure 3.2: The reaction path of the first step of hydrolysis of the pristine CHA of the four crystallographically distinguishable oxygens. The reaction has a common reactant (R-1). A first transitional state (TS-1) leads to formation of a high-energy intermediate product (IP). By inversion a second transitional state (TS-2) is reached, leading to a stable final product (P-1).

Table 3.1: Table to Figure 3.2. The first step of hydrolysis of the pristine CHA of the four crystallographically distinguishable oxygen. The mechanism of the first step has two parts. The relative activation and reaction energies of the first part (E_{Act-1}, $E_{React-1}$), second part (E_{Act-2}) and overall reaction energie ($E_{React-total}$) in kJ mol^{-1}.

The Path	E_{Act-1}	$E_{React-1}$	E_{Act-2}	$E_{React-total}$
O1	154	150	203*	23*
O2	174	140	217*	52*
O3	167	158	213*	66*
O4	163	140	217*	31*

All data marked with * have been partially or fully calculated by Mingxiu Liu. [1]

As seen in Figure 3.2. (and Table 3.1.) the activation end reaction energies of the first step differ depending on the crystallographically distinguishable oxygen. Path O1 has been chosen as the most probable path as it has the lowest activation energies for both transitional states. Furthermore, it is the least endothermic ($E_{React-total}$ = 23 kJ mol^{-1}). The O1 path has thus been chosen as a good representation and all of the rest of calculations of the hydrolysis of the pristine CHA are based on it.

---

[1] Mingxiu Liu is my coworker who has collaborated with me, especially on the first part of this project. All her work on this thesis will be acknowledged using the * mark.

3.1.2 Second Step (Q^3 to Q^2)

The first step of hydrolysis will leave the CHA unit cell with two non-equal Si Q^3 atoms, Si-I and Si-NI (see Figure 3.3). The Si-I tetrahedron has gone through an inversion in the previous step, hence the ”I” as ”Inverted”.

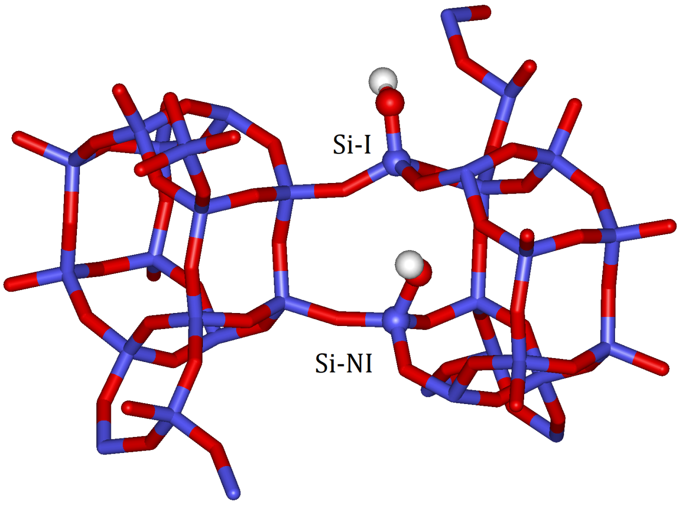

Figure 3.3: A cut-out part of a CHA cell after the first step of hydrolysis. The two Q^3 Si atoms and their respective silanol groups are marked out.

The next (second) step of hydrolysis can begin with a water molecule attacking either of the two silicon atoms. To cover both possible paths two set of calculations were performed, the $Inverted$ (I) and the $Non-Inverted$ (NI) path. The Inverted path (I) proceeds with attacking the Si atom attacked in the first step. The Non-Inverted path (NI) investigates the attack of a water molecule on the second Si atom with OH group (Si-NI) (as can be seen in Figure 3.3 and 3.4). This split can be seen in Figure 3.4.

As can be seen Figure 3.4, the Inverted path starts with a water molecule attacking the Si-I on the P-1 product. Both Si-I and Si-NI atoms are still connected to the framework by three oxygens (a Q^3 silicon atom). Thus both Inverted and Non-Inverted path of second step of hydrolysis of pristine CHA has three possible paths:

Table 3.2: Results of the second step of I and NI hydrolysis (Q^3 to Q^2) of pristine CHA. The relative activation and reaction energies of the three crystallographically distinguishable oxygens in kJ mol^{-1}.

The Path	E_{Act}	E_{React}
O1-O2-I	198*	71*
O1-O3-I	155*	35*
O1-O4-I	163*	38*
O1-O2-NI	171*	58*
O1-O3-NI	175*	71*
O1-O4-NI	151*	35*

All data marked with * have been partially or fully calculated by Mingxiu Liu.

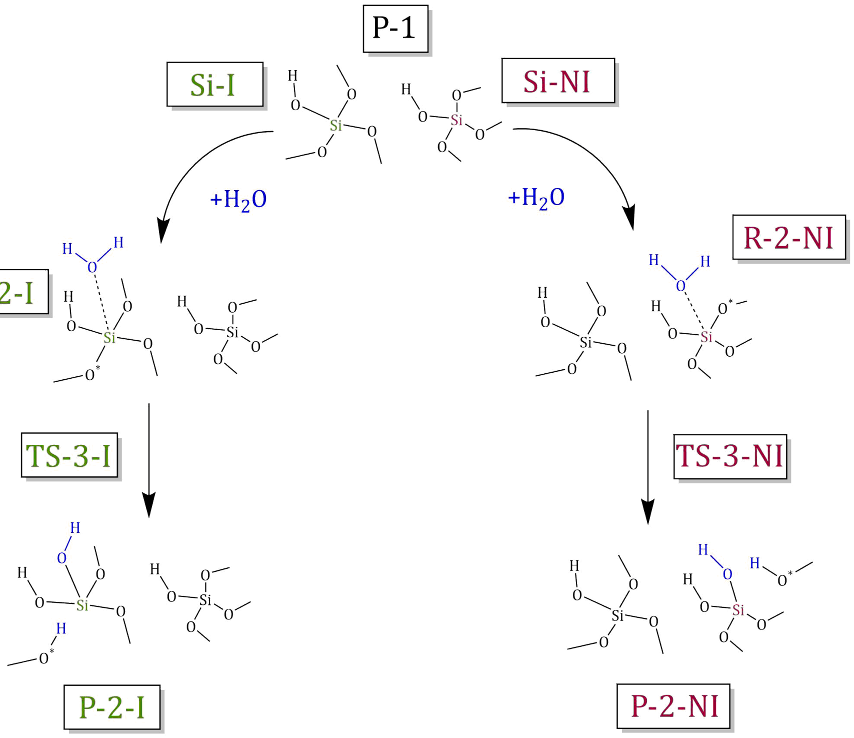

Figure 3.4: A schema showing the two possible ways the second water molecule can react with the P-1 product. Both paths can lead to total desilication of their respective atom (Si-I or Si-NI).

3.1.3 Third Step (Q^2 to Q^1)

Six possible paths for second step of hydrolysis have been found in two groups (I and NI). For the next step of hydrolysis, we choose to follow the most favourable previous path from each category, O1-O3-I and O1-O4-NI (see Table 3.2). The activation energies of the paths O1-O3-I and O1-O4-NI are very similar (155 and 151 kJ mol^{-1}, respectively), so both were investigated further. After the second step of hydrolysis, the Si-NI and Si-I atoms had been attached via two oxygen atoms to the framework (they are Q^2 Si atoms). The third step of hydrolysis had therefore two possible paths (both for I and NI).

A molecule of water had been added to the product of the O1-O3-I and O1-O4-NI path. Four transitional states were obtained.

Table 3.3: Results of the third step of I and NI hydrolysis (Q^2 to Q^1) of pristine CHA. The relative activation and reaction energies of the two crystallographically distinguishable oxygens in kJ mol^{-1}.

The Path	E_{Act}	E_{React}
O1-O3-I-O2	137	37
O1-O3-I-O4	161	-2
O1-O4-NI-O2	100	71
O1-O4-NI-O3	124	35

Both paths are again relatively comparable. The activation energies of the best possible paths are 137 and 100 kJ mol^{-1}, for I and NI respectively. The NI path has a smaller E_{Act} in this step, mostly due to starting with a less stable reactant.

3.1.4 Fourth Step (Q^1 to Q^0)

The fourth step of the hydrolysis leads to total desilication, the complete detachment of a Si atom (see Figure 3.5)). This step can have only one possible path. The O1-O3-I-O2 and O1-O4-NI-O3 were selected as reactants for the last step of hydrolysis.

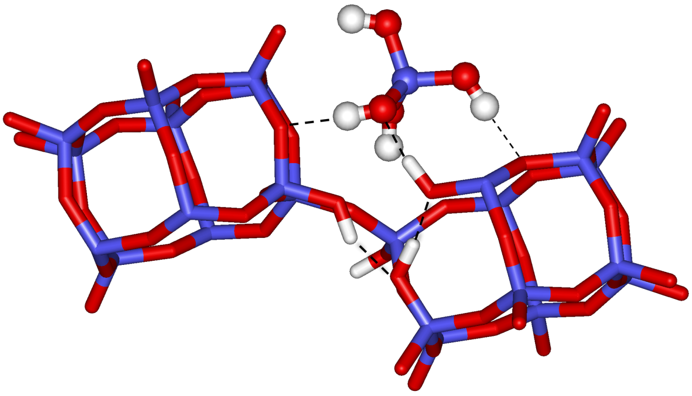

Figure 3.5: A cut-out of a CHA unit cell with the O1-O4-NI-O2-O4 product. A SiO_4H_4 tetrahedron is detached from the framework. However, it stays close to the framework as the SiO_4H_4 and the rest of the framework interact via hydrogen bonding. The structure is thus stable (see Figure 3.6).

The only possible paths following the O1-O3-I-O2 and O1-O4-NI-O2-O4 product:

Table 3.4: Results of the fourth, last step of hydrolysis of pristine CHA. The relative activation and reaction energies for the only possible oxygen leading to total desilication in kJ mol^{-1}.

The Path	E_{Act}	E_{React}
O1-O3-I-O2-O4	92	-43
O1-O4-NI-O3-O2	132	-73

3.2 Pristine CHA - Summary

The results presented in the section above are separated to four steps. After the first step the reaction mechanism splits in two non-equal paths (I and NI, see Figure 3.4). Both paths are available options in terms of hydrolysing a pristine CHA. For a better comparison of the two paths, the relative energies have been plotted in Figure 3.6. The most energetically favorable paths from both I and NI paths have been chosen. The whole reaction can be summarised by this equation:

$$\mathrm{CHA_{pristine}} + 4\mathrm{H_2O} \longrightarrow \mathrm{CHA_{defective}} + \mathrm{SiO_4H_4}. \tag{3.1}$$

Each step of hydrolysis require an adsorption of a water molecule. The water molecule was treated as if adsorbed from gas phase. Therefore the transition in between P-X and R-(X+1) represents a water adsorption on the system. As can be seen in Figure 3.6 this is almost always exothermic. The formed SiO_4H_4 remains in the CHA canal. It interacts with the CHA framework via hydrogen bonds which increase the stability of the final product.

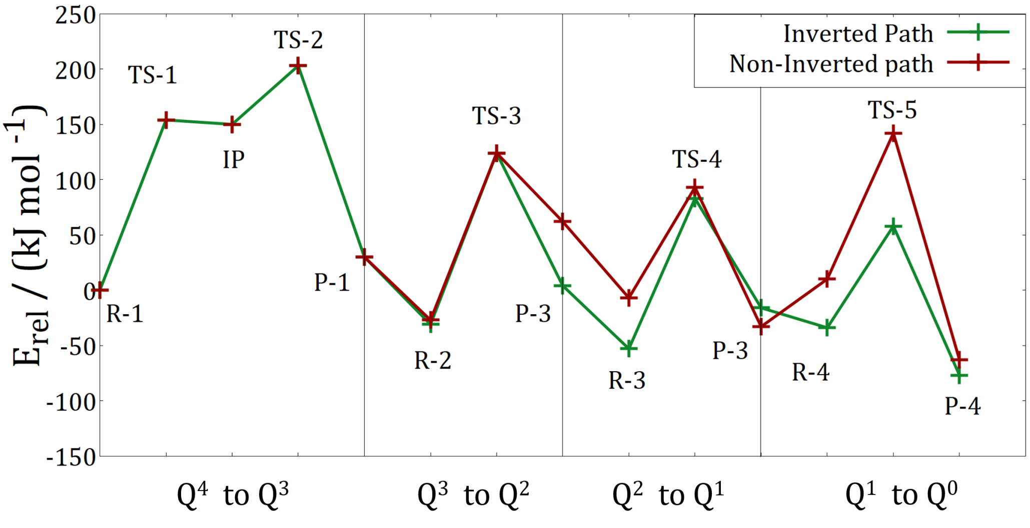

Figure 3.6: A plot of relative energies (in kJ mol^{-1}) of the most energetically favorable paths (NI and I) leading to total desilication of pristine CHA. Both paths go through the same first step. They split on the second step (P-1 is the last common structure).

Table 3.5: Table to Figure 3.6. The relative activation and reaction energies of both paths in kJ mol^{-1}. The Inverted and the Non-Inverted paths share first four energies.

The step	Inverted	Non-Inverted
R-1 to TS-1	154	
TS-1 to IM	-4	
IM to TS-2	53	
TS-2 to P-1	-174	
P-1 to R-2	-61	-57
R-2 to TS-3	155	151
TS-3 to P-2	-117	-62
P-2 to R-3	-60	-90
R-3 to TS-4	137	100
TS-4 to P-3	-100	-129
P-3 to R-4	-18	-43
R-4 to TS-5	92	132
TS-5 to P-4	-135	-205

All the obtained TS on all paths had a very similar geometry of the reacting atoms. The water molecule attaches onto a Si atom. This leads to a partial deformation of the Si tetrahedron. The structure of the TS resembles a deformed trigonal bipyramid, with (5) oxygens in the vertices, as can be seen in Figure 3.7.

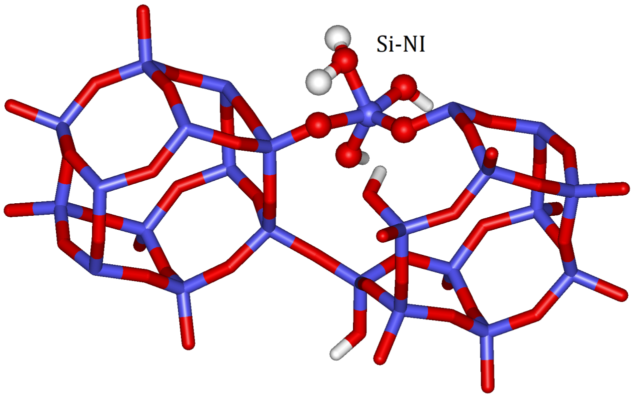

Figure 3.7: A cut-out of a CHA unit cell with the O1-O4-NI-O2 transition state. The deformed trigonal bipyramid is marked out. All other obtained TS were qualitatively similar.

In all steps the paths have different activation and reaction energies. Energy of a TS heavily depends on geometry of the reacting atoms, but is influenced by the surrounding structure as well. Although geometry of the reacting atoms of all paths in all steps is fairly similar, the overall topology differs. If an already existing silanol group can interact with the new water molecule, the TS is stabilised. An example of this effect can be well shown on the O1-O4-NI-O3-O2 TS (see Figure 3.8).

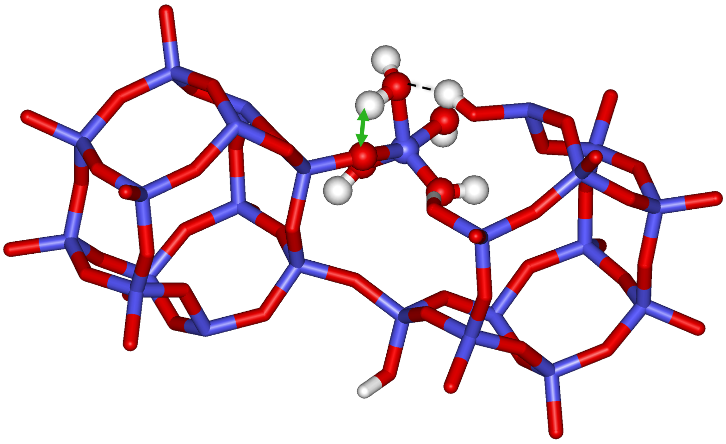

Figure 3.8: A cut-out of a CHA unit cell with the O1-O4-NI-O3-O2 TS. The deformed trigonal bipyramid and an interacting hydrogen are marked out. A previously introduced OH group can be seen forming a hydrogen bond with the attached water molecule. This helps to stabilise the TS. The green arrow shows the direction of the proton transfer.

This trend is more significant for later steps, as more silanol groups can interact. Moreover, as the hydrolysis proceeds the Si tetrahedra can change conformation more easily, so the Si tetrahedra can accommodate the water molecule more easily and stabilise the TS. This overall trend can be seen especially with the I path in Figure 3.6. Note how the activation energies tend to decrease for later steps.

3.3 Defected CHA

A silanol nest can be created by removing a single T-atom (Si in this case) out of the zeolitic framework and adding hydrogens in place of the T-atom (see Figure 3.9 and Figure 3.10). The silanol nest is strongly stabilised via a system of four hydrogen bonds.

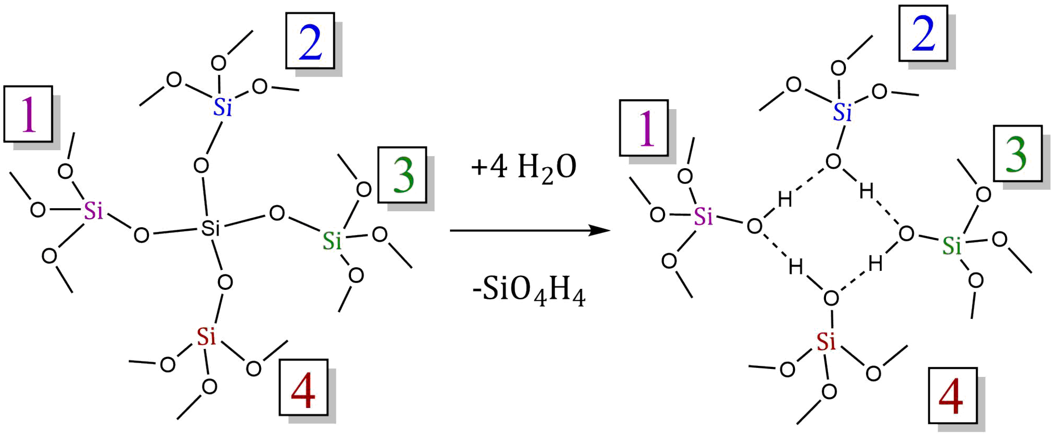

Figure 3.9: A schematic depiction of a pristine CHA and a defected CHA with silanol nest. The silanol nest is surrounded by four crystallographically distinguishable T-atoms (1,2,3 and 4).

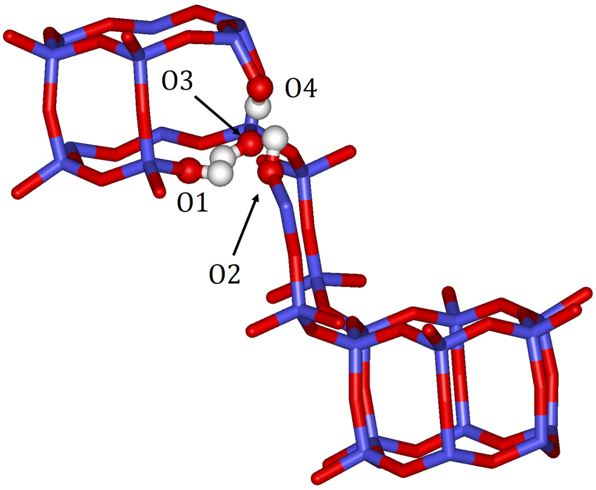

Figure 3.10: A cut-out of CHA unit cell with the silanol nest defect. The OH groups forming the nest are marked and numbered. Note the interaction of silanol groups.

The hydrolysis of a defected CHA starts with a water molecule attacking one of the four crystallographically distinguishable surrounding Si atoms. Therefore, it was necessary to consider hydrolysis on all four Si atoms. For the purposes of the calculations, the Si atoms have been labeled 1,2,3 and 4, in respect to their crystallographic position relative to the central Si atom (which is now not present).

3.3.1 First step (Q^3 to Q^2)

The Si atoms surrounding the silanol nest are still attached to the framework via three O atoms (they are Q^3 Si atoms). So a total of 12 paths are possible for the first step.

Table 3.6: A first step (Q^3 to Q^2) of hydrolysis of a defected CHA. All 12 possible paths have been calculated. All the activation and reaction energies are reported in kJ mol^{-1}.

The Path	E_{Act}	E_{React}
O1-O2	155*	58*
O1-O3	170*	75*
O1-O4	186*	28*
O2-O1	137*	25*
O2-O3	123*	58*
O2-O4	108*	26*
O3-O1	113	28
O3-O2	100	47
O3-O4	173	39
O4-O1	171*	29*
O4-O2	148*	43*
O4-O3	168*	55*

All data marked with * have been partially or fully calculated by Mingxiu Liu.

The geometry of the obtained TS resembles a deformed trigonal bipyramid, much like in the pristine section of calculations (see Figure 3.7). Same as seen previously, (see Section 3.1) the activation energies depend greatly on the crystallographically distinguishable oxygen. In the case of the defected CHA, the TS are different mostly due to their ability to interact with the silanol nest. The silanol nest is a very stable structure. Therefore, if the TS deforms the already existing system of hydrogen bonds, the activation energies is going to be high. On the other hand, if the adsorbed water molecule can form a new hydrogen bond with the nest, the TS is stabilised and the E_{Act} is going to be lower. This can be seen on the O3-O2 TS, which is the most favourable (see Figure 3.11).

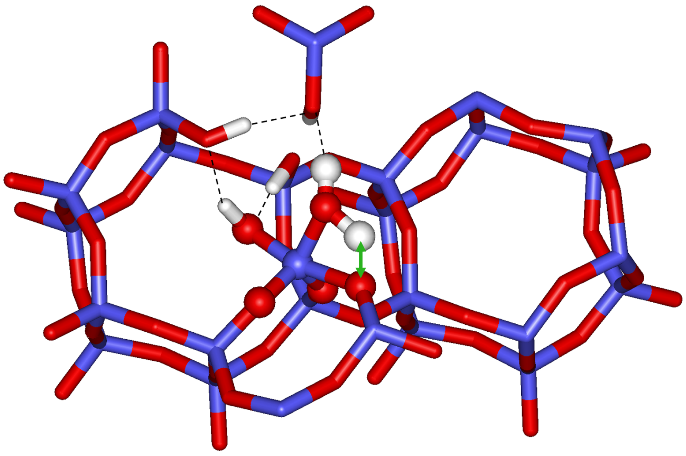

Figure 3.11: A cut-out CHA unit cell with the O3-O2 TS. The atoms forming the deformed trigonal bipyramid are marked. A system of hydrogen bonds is highlighted via dashed lines. The interaction of the attacking water molecule and the silanol nest greatly stabilises the TS. The green arrow shows the direction of the proton transfer.

In some paths the direct product of hydrolysis is not very stable. The system could then achieve a more stable product via one or more steps. This can be seen on the reconfiguration of the O2-O4 product (see Figure 3.12).

This post-hydrolysis reconfiguration is, however, hindered only by much smaller energetic barriers (see Figure 3.12). In Table 3.6 only the E_{React} relative to the most stable product has been reported.

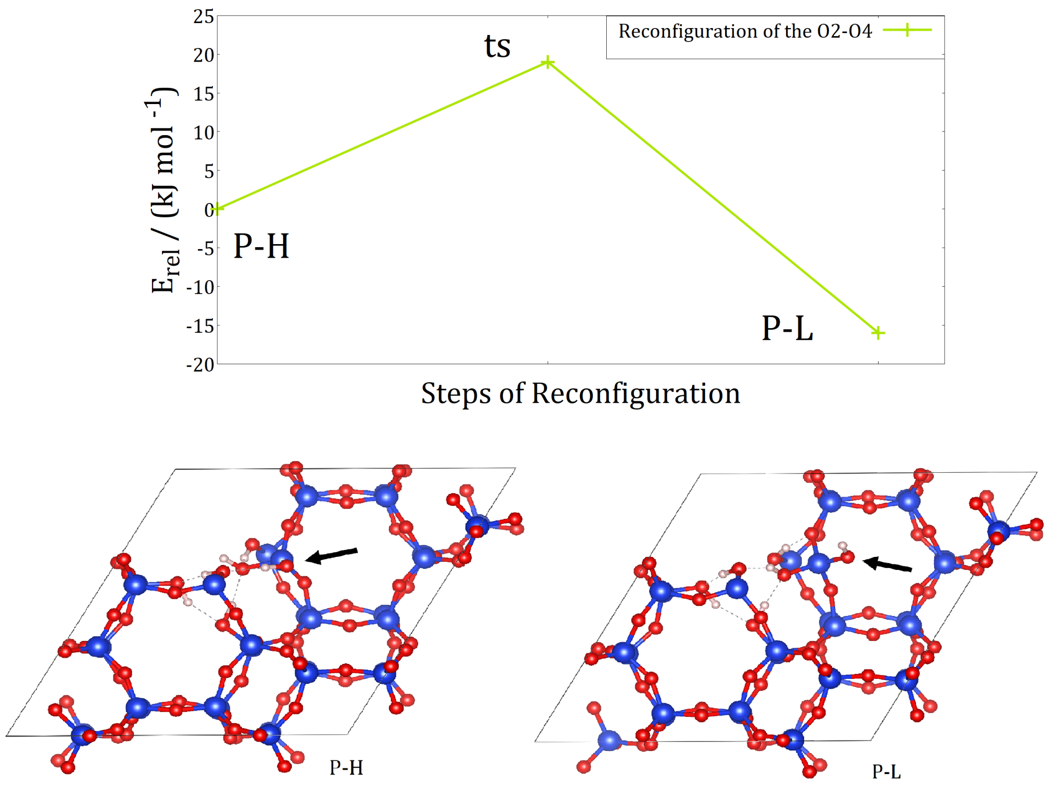

Figure 3.12: The O2-O4 product of hydrolysis (P-H) can achieve a more stable geometry (P-L) via a rotational transitional state (ts). A Si tetrahedron (marked by the arrow) rotates and forms a more favourable product. As can be seen the energetic barrier is insignificant in comparison with the barrier of the hydrolysis itself.

3.3.2 Second Step (Q^2 to Q^1)

As can be seen in Table 3.6 paths with lowest E_{Act} are O2-O3, O2-O4, O3-O1 and O3-O2. Thermodynamically, these paths are the most probable. Since each of the four products is still connected via two oxygens to the framework, eight paths have been studied.

Table 3.7: A second step (Q^2 to Q^1) of hydrolysis of a defected CHA. Eight possible paths for this step following the most favourable product of the first step. All reported energies are in kJ mol^{-1}.

The Path	E_{Bar}	E_{Act}	E_{React}
O2-O3-O1	160	110	80
O2-O3-O4	193	193	29
O2-O4-O1	112	112	31
O2-O4-O4	150	145	20
O3-O1-O2	118	118	73
O3-O1-O4	143	143	50
O3-O2-O1	118	118	98
O3-O2-O4	113	113	-19

All TS obtained for this chapter had the deformed trigonal bipyramid geometry (see Figure 3.11). The activation energy of a given path can be linked with water molecule interacting with silanol nest. Some TS are significantly stabilised by this effect.

3.3.3 Third Step (Q^1 to Q^0)

The third and last step leads to a total desilication of the respective Si atom. The detached SiO_4H_4 tetrahedron tends to stay in the proximity of the silanol nest, as SiO_4H_4 and the framework can interact with it via hydrogen bonding (see Figure 3.13).

As can be seen in Table 3.7, the paths in the previous step vary a lot in terms of E_{Act}. The following paths have been chosen to be investigated further: O2-O3-O1, O2-O4-O1, O3-O1-O2, O3-O2-O1 and O3-O2-O4. In each case, the Si atom is linked to the framework only by one oxygen. Thus the last step has only one possible path for each product.

Table 3.8: A third step (Q^1 to Q^0) of hydrolysis of a defected CHA, leading to total desilication. Five products of the previous step (Q^2 to Q^1) have been chosen. All energies are reported in kJ mol^{-1}.

The Path	E_{Act}	E_{React}
O2-O3-O1-O4	157	27
O2-O4-O1-O3	199	13
O3-O1-O2-O4	166	26
O3-O2-O1-O4	131	7
O3-O2-O4-O1	152	-4

As seen in Table 3.8 the O3-O2-O1-O4 path is the path with lowest E_{Act} while being only slightly endothermic. It is thus the most likely path for the last step of hydrolysis.

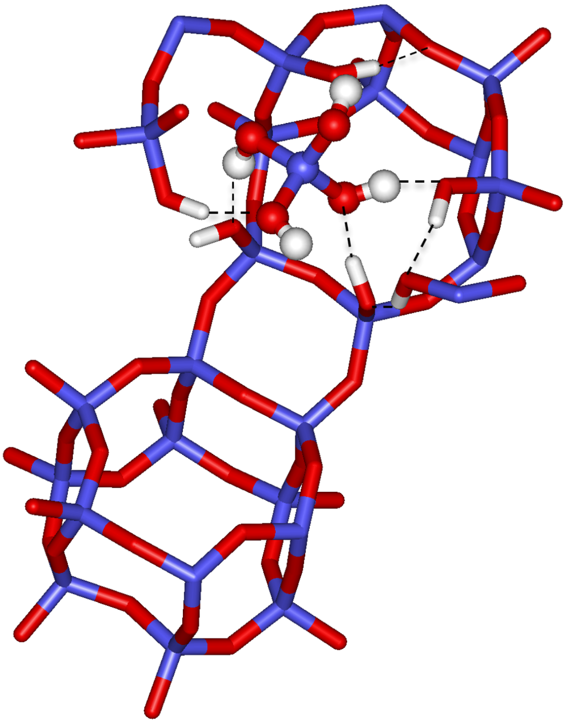

Figure 3.13: A cut-out of CHA unit cell with the detached SiO_4H_4 tetrahedron, product of the O3-O2-O1-O4 path. The SiO_4H_4 tetrahedron interacts with the silanol nest and with the introduced OH groups, thus stabilising the structure.

3.4 Defected CHA - Summary

Five possible paths leading to total desilication have been calculated. The total desilication of a defected CHA can be represented by this equation:

$$\mathrm{CHA}_{\mathrm{defected}}(\mathrm{OH}_4) + 3\mathrm{H}_2\mathrm{O} \longrightarrow \mathrm{CHA}_{\mathrm{defected}}(\mathrm{OH}_6) + \mathrm{SiO}_4\mathrm{H}_4. \tag{3.2}$$

Each step of hydrolysis requires a single molecule of water to be adsorbed to the structure. Each of the water molecule was treated as if adsorbed from gas phase. Every transition in between P-(X) and R-(X+1) represents a water adsorption, and the energy difference is the energy of the adsorption.

Overall, it can be said that the O3-O2-O1-O4 is the most favourable path. In the first step, it has the lowest E_{Act} out of all 12 paths (see O3-O2 in Table 3.6). In the second step, it has again comparably low activation energy (see O3-O2-O1 in table Table 3.7). In the last step, it has the lowest E_{Act}. In fact, the path with second lowest E_{Act} has its activation energy 21 kJ mol^{-1} higher than O3-O2-O1-O4 path (see Table 3.8). In order to give a better overview of the path, all three steps have been plotted in Figure 3.14 .

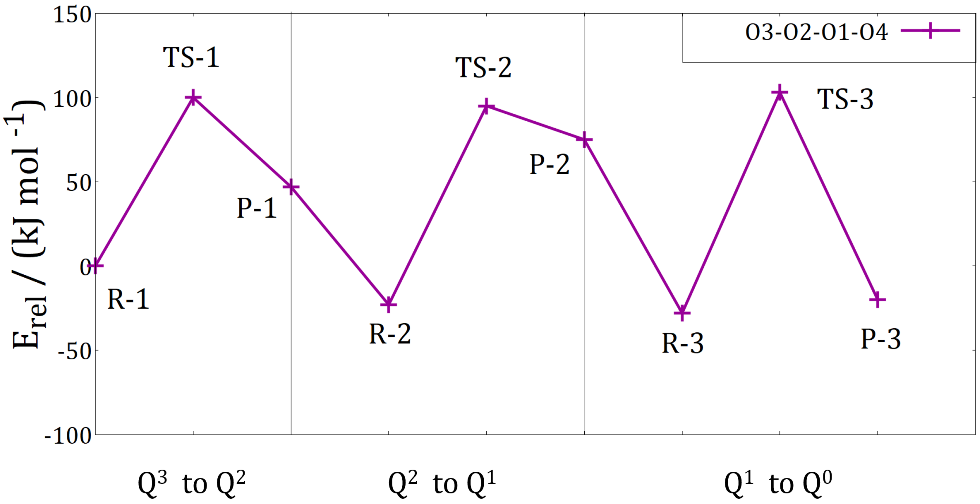

Figure 3.14: A plot of the O3-O2-O1-O4 path of total desilication of defected CHA in kJ mol^{-1}. The path has to overcome a series of three TS (TS-1 to TS-3). The last step has the largest activation energy (E_{Act} = 131 kJ mol^{-1}) The process is overall slightly exothermic. The final product is stable.

Table 3.9: Table to Figure 3.14. The relative activation and reaction energies of the O3-O2-O1-O4 path in kJ mol^{-1}.

The step	O3-O2-O1-O4
R-1(SN) to TS-1(SN)	103
TS-1(SN) to P-1(SN)	-53
P-1(SN) to R-2(SN)	-73
R-2(SN) to TS-2(SN)	118
TS-2(SN) to P-2(SN)	-20
P-2(SN) to R-3(SN)	-103
R-3(SN) to TS-3(SN)	131
TS-3(SN) to P-3(SN)	-124

4. Discussion of the Results

In Sections 3.3 and 3.1 two data sets have been presented, The Pristine and Defected CHA data sets. This section will be focused on comparing the two data sets.

The Pristine data cover a reaction spreading over four steps, meanwhile, the Defected CHA data sets only three steps. All atoms in a pristine CHA unit cell are Q^4 atoms, but a Si atom next to the silanol nest starts as Q^3 atom, so an extra step is needed to hydrolyse a pristine CHA, as seen in Figure 4.1.

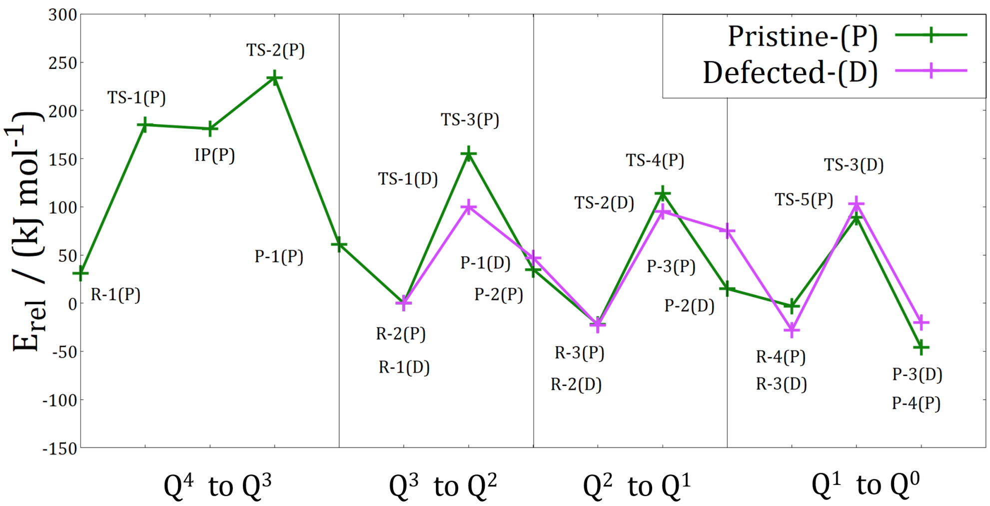

Figure 4.1: Comparison of the two most favourable paths of Pristine and Defected CHA data sets, Inverted and O3-O2-O1-O4 paths respectively. The Defected path starts with a Q^3 Si atom, therefore, begins with the Q^3 to Q^2 section. The relative energies are in kJ mol^{-1}. The relative energies of Pristine path have been shifted up, so R-2(P) and R-1(D) would both be equal to zero, for easier comparison of the data.

Figure 4.1 is a comparison of the most favourable paths for each data set, for the Inverted path on Pristine CHA (labeled (P)) and the O3-O2-O1-O4 path on Defected CHA (labeled (D)). The Q^4 to Q^3 step is the step with the highest E_{Act}. It can be argued that the Q^4 to Q^3 step is split in two reactions, thus splitting the total energy in two barriers; E_{Act} for R-1(P) to IP(P) is 154 kJ mol^{-1}, E_{Act} for IP(P) to P-1(P) is 53 kJ mol^{-1}. However the E_{Act} for a reverse reaction from IP(P) to R-1(P) is only 4 kJ mol^{-1}. The IP(P) is thus going to be scarcely populated, slowing the rate of the Q^4 to Q^3 step of the reaction even further.

The hydrolysis of Defected CHA is clearly advantageous as it can start without overcoming Q^4 to Q^3 step. Furthermore, the Q^3 to Q^2 step is significantly less demanding for the Defected CHA. The next step, the Q^2 to Q^1 step of hydrolysis is again less demanding for Defected CHA.

However, the last step, Q^1 to Q^0 is less demanding for the Pristine CHA. Moreover, the product P-4(P) is significantly more stable than P-3(D). In fact, the Q^1 to Q^0 is the most demanding step for the entire Defected path. It is likely that the Q^1 to Q^0 step will be a bottleneck step of the Defected CHA path. The low stabilisation of the P-3(D) end product can lead to the reaction going backwards and healing the disconnected bond. Recent research using marked $H_2^{17}O$ water and Solid state NMR has shown the ability of zeolite, in some cases, to heal once disconnected bonds.[7] It is important to note that the problem is still not completely understood and is a subject of ongoing research.

On the other hand, the Pristine CHA path has a tendency to have lower barriers as it progresses, which is in agreement with other computational studies. [7] Furthermore the final product P-4(P) is stable, making the backwards reaction unlikely. If the system overcomes the first most demanding step it will probably have a tendency to lead up to total desilication.

For the Defective path, the good accessibility of the Q^3 to Q^2 and Q^2 to Q^1 steps in combination with an energetically demanding last step (Q^1 to Q^0) can mean that the Si atom stays in Q^1 form for a prolonged periods of time. As the hydrolysis proceeds elsewhere, a larger extra-framework species can form as $(OH)_3Si - Si(OH)_3$ dimer or perhaps even a larger clusters. There, however, seems to be no experimental evidence of such formations in zeolites.

Thus far, we have only focused on the best possible paths. In order to get a better grasp of the entire data set, the arithmetic mean of the obtained data can help. The arithmetic mean of the E_{Act} for both the Pristine and Defected will be discussed first.

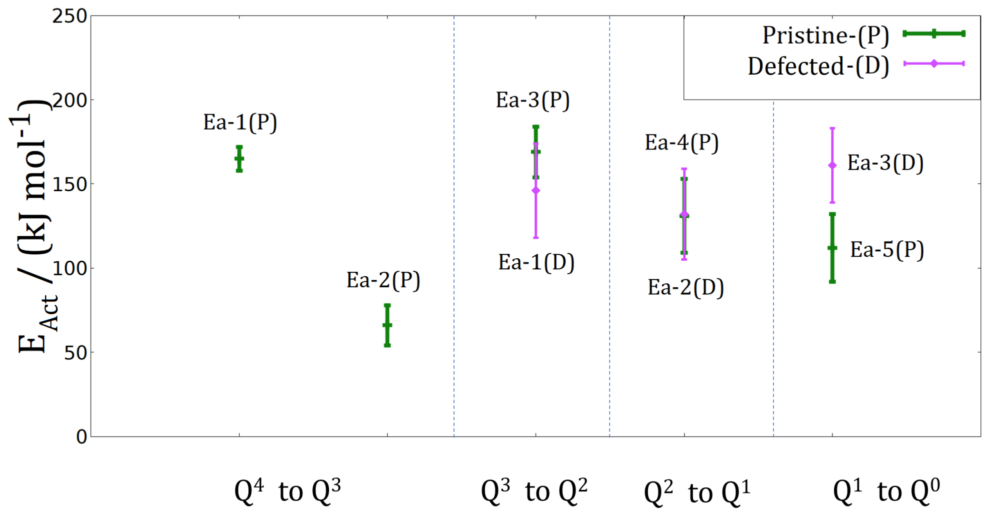

Figure 4.2: A plot of the arithmetic mean of the E_{Act} for Pristine (P) and Defected (D) data set. The statistic has been made from all obtained data (of every step). The margins of errors are marked.

Figure 4.2 is a comparison of both Pristine and Defected data sets. The arithmetic means of the E_{Act} are presented for the each steps of reactions (like in Figure 4.1). Firstly, it should be noted that most of the trends discussed above (for the best possible paths) are valid for the arithmetic means of the E_{Act} as well (see Table 4.2). Note that the Q^4 to Q^3 has two steps, thus two activation energies. As mentioned above, the Q^4 to Q^3 step presents a difficult barrier to overcome as the TP(P) (in Figure 4.1) is minimally stabilised. As discussed above, the Defected data set doesn't have to overcome the first step of hydrolysis.

The Q^3 to Q^2 is more advantageous for the Defected data sets even though the margins of error overlap. This mirrors, what can be seen for the best paths in Figure 4.1. Note Ea-3(P) is the highest activation energy for a single step reaction for the entire process (see Table 4.2).

Table 4.1: Table to Figure 4.2. The arithmetic mean of E_{Act} and the standard deviation σ in kJ mol^{-1}.

The Point	The Arithmetic Mean	σ
Ea-1(P)	165	7
Ea-2(P)	66	12
Ea-3(P)	169	15
Ea-4(P)	121	22
Ea-5(P)	112	20
Ea-1(D)	146	28
Ea-2(D)	132	27
Ea-3(D)	161	22

The average E_{Act} for the Q^2 to Q^1 step is for both data sets similar, the Pristine data set is slightly more favourable. The arithmetic mean of E_{Act} the Pristine and Defected data set is 121 and 132 kJ mol^{-1}. This goes against what we have seen for the best possible paths in Figure 4.1, where the Defected data set was clearly advantageous.

The last step of hydrolysis, the Q^1 to Q^0 step, is clearly advantageous for the Pristine data set. It is important to note that only two paths of the last steps of hydrolysis for the Pristine data set have been calculated. The statistics of the Ea-5(P) should therefore be approached with caution.

Overall, a trend of the E_{Act} gradually getting lower can be observed. Further cementing the idea that the first step is the rate determining step of the hydrolysis on the Pristine system. As the barriers get lower, the reaction will probably have a tendency to run to completion, i.e. to total desilicatio. The Defected data set is obviously advantageous, as it doesn't have to overcome the demanding Q^4 to Q^2. The activation energies, however, have tendency to get higher as the hydrolysis progresses. This means that reaction might stop before completion, as discussed above.

The average E_{React} will be discussed next.

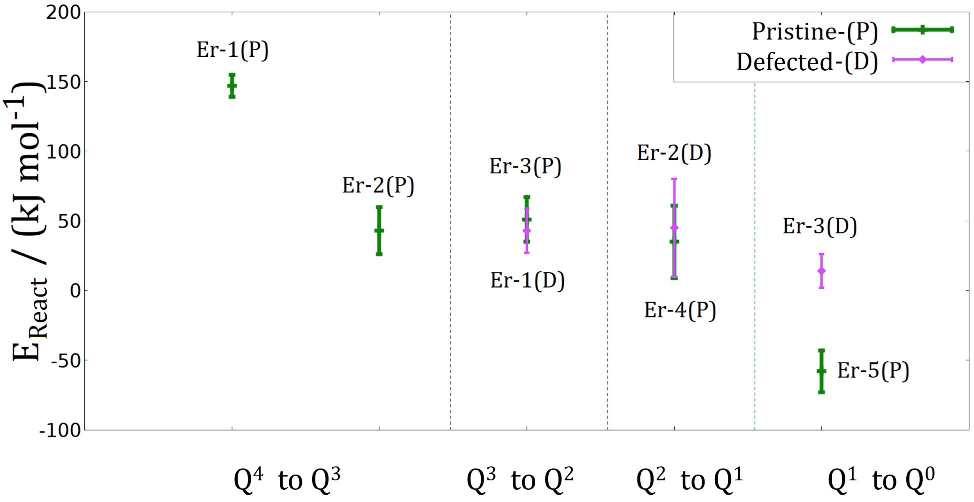

Figure 4.3: A plot of the arithmetic mean of the E_{React} for Pristine (P) and Defected (D) data set. The statistic has been made from all obtained data (of every step). The margins of errors are marked.

Table 4.2: Table to Figure 4.3. The arithmetic mean of E_{React} and the standard deviation σ in kJ mol^{-1}.

The Point	The Arithmetic Mean	σ
Er-1(P)	147	8
Er-2(P)	43	17
Er-3(P)	51	16
Er-4(P)	35	26
Er-5(P)	-58	15
Er-1(D)	43	16
Er-2(D)	45	35
Er-3(D)	14	12

Figure 4.3 compare the E_{React} of both Pristine and Defected data set. Again much that has been discussed above (for the two best paths of hydrolysis, Figure 4.1) holds for the average values of the E_{React} as well.

The first step of hydrolysis Q^4 to Q^3 has a two step mechanism with a high-in-energy intermediate product, the Er-1(P) correspond to the formation of the intermediate product (IP(P)) in Figure 4.1). Overall E_{React}, Er-2(P) is not that high and Q^4 to Q^3 is only slightly endothermic.

The average E_{React} for Q^3 to Q^2 step are similar for both data sets. The margins of error have a large overlap. The same can be said for the Q^2 to Q^1 step, although the Pristine data set is a bit lower in energy.

The last step Q^1 to Q^0 is, however, very different. The last step is noticeably exothermic for the Pristine data set. The E_{React} of the Defected data set is the lowest for the last step it is still endothermic.

Looking at the average E_{React}, we can again recognise some trends. Firstly, the average E_{React} of the Pristine data set is gradually lower as the hydrolysis progresses, from being highly endothermic to being significantly exothermic. The negative E_{React} is mostly due to the formation of the silanol nest, which stabilises the system. Secondly, we can see that E_{React} of the Defected data does not change all that much as the hydrolysis progress. The E_{React} for the last step is admittedly lower, though. This correspond to the ideal path (Figure 3.14).

It would seem the silanol nest itself has a major role in the trends discussed in this section. The Pristine data will be discussed first.

The E_{Act} and the E_{React} of the Pristine data shows tendency to decrease over the course of hydrolysis. As more OH groups are introduced, the attacking water molecule can interact with the framework more easily, forming more stable TS. The gradual formation of the silanol nest leads to more stable products and lower E_{React}. The two phenomenons seem to effect especially the last step of pristine CHA hydrolysis, Q^1 to Q^0 step.

The defected system is in a different situation. The silanol nest has already been formed and it can influence the E_{Act} and the E_{React} both ways. If the incoming water molecule can interact with the nest without deforming it, the E_{Act} will be generally low (only 100 kJ mol^{-1} for the most favourable path). If the water molecule needs to deform or disturb the system of hydrogen bonds to be able to form, the TS E_{Act} will be significantly higher.

This can be seen for the product as well. Hydrolysing the Si atoms surrounding the silanol nest will influence the stability of the nest as well, leading to higher E_{React}.

This study was limited to finding mechanisms with a single water molecule in the zeolit chanel. This is a reasonable assumption as the temperature of the zeolite dictates the equilibrium water loading, the amount of water that is present in zeolite (the number of water molecules per unit cell) under given condition. Under the temperatures this thesis aims to study, (such as present in a FCC process $\sim$ 700 C° [33]), the water loading is very low. Thus making mechanisms involving multiple waters highly unlikely to happen. Multimolecular mechanisms have, however, been reported for higher water loading and low temperatures.[28] [7]

Only some paths have been selected and calculated to the last step. The paths with high activation energies were deemed unlikely and, thus uninteresting. The discarded paths, however, could have had more interesting or favourable next steps. This decision was made to reduce the overall number of TS that had to be calculated. Calculating all the possible paths would give a more complete data set and would give a better picture of the hydrolysis. The discarded paths, however, would always lag behind the most favourable paths as the rate of a reaction is determined by the slowest (most demanding) step. Moreover, in many cases the paths directly compete, making the paths with higher barriers even more unlikely.

Conclusion

A theoretical DFT-based study of the influence of silanol nest on hydrolysis of CHA has been performed. Two models were considered, a defected CHA containing the silanol nest defect and a pristine CHA for reference. Both systems were extensively researched to consider a large number of possible paths of hydrolysis. A total desilication has been reached on both models.

It was shown that the path of hydrolysis highly depends on the crystallographically distinguishable oxygens surrounding the given path. The most favourable paths have been discovered and the rate determining steps have been recognised.

The obtained data met the experimentally set expectations that a silanol nest defect enhances the hydrolysis of the system. It has been shown that the most demanding step of the hydrolysis is Q^4 to Q^3, which is not necessary for the system with a silanol nest. Moreover two of the three remaining steps toward desilication have a lower activaton energy for the defected CHA. As this thesis aimed to study hydrolysis under high temperatures, the water molecule will have enough thermal energy to overcome basically all of the proposed barriers. However, it is reasonable to expect that the rate of hydrolysis will be significantly higher for a system containing the silanol nest.

My coworker Mingxiu Liu, whom has done some of the calculation presented, currently studies hydrolysis of MFI, a different zeolite structure. Her results, though yet unfinished, seem to be in agreement with this study. The silanol nest seems to promote hydrolysis on MFI in a similar way it does on CHA. In extent, it is reasonable to expect other zeolites to behave similarly and that our findings for CHA can be generalised for other zeolites.

The simple static calculation used in this thesis gives us the electronic energy of the system. Even without any thermal correction electronic energy, gives an important insight about the energetic of chemical reactions. To get a realistic idea about the kinetics of the system, a more advanced method would have to be used, like the microkinetic analysis. Performing a dynamic study, e.g. such as some form of *ab inito* MD calculation generally give a better and more complex mapping of the PES. Using *ab inito* MD calculation wuld make for an interesting and promising follow-up research.

Bibliography

[1] P. A. Wright. *Microporous Framework Solids.* RSC Publishing: 553 Cambridge, Cambridge, 2008.

[2] Nachtigall P. Čejka J., Morris R. E. *Zeolites in Catalysis.* The Royal Society of Chemistry, London, 2017.

[3] Johannes H. Bitter Krijn P. de Jong Sander van Donk, Andries H. Janssen. Generation, characterization, and impact of mesopores in zeolite catalysts. *Catalysis Reviews*, 45:297–319, 2003.

[4] Petracovschi E. Kerber T. Sauer J. Silaghi M., Chizallet C. and Raybaud P. Regioselectivity of alo bond hydrolysis during zeolites dealumination unified by brønstedevanspolanyi relationship. *ACS Catalysis*, 5(1):11–15, 2015.

[5] Sauer J. Raybaud P. Silaghi M., Chizallet C. Dealumination mechanisms of zeolites and extra-framework aluminum confinement. *Journal of Catalysis*, 339(2):242–255, 2016.

[6] Honglin Chen · Xiaoming Zhang Yuling Ye Mengqin Yao. Influence of silanol defects of zsm-5 zeolites on trioxane synthesis from formaldehyde. *Catalysis Letters*, 150:1445–1453, 2020.

[7] F. Uhlík Mariya Shamzhy Maksym Opanasenko J. Čejka Christopher J. Heard, Lukáš Grajciar and P. Nachtigall. Zeolite (in)stability under aqueous q3 or steaming conditions. *Advanced Materials*, 2003264:1–29, 2022.

[8] Errol G. Lewars. *Computational Chemistry.* The Royal Society of Chemistry, Switzerland, 2016.

[9] Kohn W. Hohenberg P. Inhomogeneous electron gas. *Physical Review*, 136:864–871, 1964.

[10] H.Englisch R.Englisch. Hohenberg-kohn theorem and non-v-representable densities. *Physica A*, 121A:253–268, 1983.

[11] Sham L. J. Kohn, W. Self-consistent equations including exchange and correlation effects. *Physical Review*, 140:1133–1138, 1965.

[12] Kieron Burke and friends. The abc of dft,://dft.uci.edu/doc/g1.pdf.

[13] Max C. Holthausen Wolfram Koch. *A Chemist's Guide to Density Functional Theory.* Wiley-VCH, 2001.

[14] John P. Perdew Paul Zieschea, Stefan Kurthb. Density functionals from lda to gga. *Computational Materials Science*, 11:122–127, 1998.

[15] Matthias Ernzerhof John P. Perdew, Kieron Burke. Generalized gradient approximation made simple. *Physical Review Letters*, 77(18):3866–3868, 1996.

[16] S.Lundqvist and N.H.March. *Theory of the Inhomogeneous Electron Gas.* Springer Science+Business Media, LLC, New York, 1983.

[17] Stephan Ehrlich Helge Krieg Stefan Grimme, Jens Antony. A consistent and accurate ab initio parametrization of density functional dispersion correction (dft-d) for the 94 elements h-pu. *The Journal of Chemical Physics*, 132(154104), 2010.

[18] Lars Goerigk Stefan Grimme, Stephan Ehrlich. Effect of the damping function in dispersion corrected density functional theory. *The Journal of Chemical Physics*, 32:1456–1465, 2011.

[19] Mutasem Odeh. About the quantum mechanics of the electrons in crystal lattices. *Solid State Physics Project*, (211A), 2018.

[20] Ricardo Grau-Crespoc Aron Walshd Ian J.Busha C. Richard A. Catlowc Scott M. Woodley Asimina Maniopouloua, Erlend R.M. Davidsonb. Introducingk-point parallelism into vasp. *Computer Physics Communications*, 183:1696–1701, 2012.

[21] J. Kohanoff. *Electronic Structure Calculations for Solids and Molecules: Theory and Computational Methods.* Cambridge University Press, New York, 2006.

[22] David Wales. *Energy Landscapes.* Cambridge University Press, Cambridge, 2013.

[23] Jiří Kopáček. *Matematická analýza nejen pro fyziky.* MatfyzPress, Praha, 2015.

[24] Heinrich L.Selzle Pavel Hobza and Edward W.Schlag. Potential energy surface of the benzene dimer: Ab initio theoretical study. *Journal of the American Chemical Society*, 116:3500–3506, 1994.

[25] Mills G. Jacobsen K.W. Jónsson, H. *Classical and Quantum Dynamics in Condensed Phase Simulations,.* World Scientific, 1998.

[26] H. Jónsson G. Henkelman, B.P. Uberuaga. A climbing image nudged elastic band method for finding saddle points and minimum energy paths. *J. Chem. Phys.*, 113:9901–9904, 2000.

[27] H. Jónsson G. Henkelman. A dimer method for finding saddle points on high dimensional potential surfaces using only first derivatives. *The Journal of Chemical Physics*, 111:7010–7022, 1999.

[28] Cameron M. Rice Suzi M. Pugh Petr Nachtigall Sharon E. Ashbrook 2 Christopher J. Heard, Lukas Grajciar and Russell E. Morris. Fast room temperature lability of aluminosilicate zeolites. *Nature Communications*, 10:1–10, 2019.

[29] Ch. Baerlocher and L.B. McCusker. Database of zeolite structures,http://www.iza-structure.org/databases/.

[30] J. Furthmüller G. Kresse. Efficient iterative schemes for ab initio total-energy calculations using a plane-wave basis set. *Physical Review*, 54(16):11 169–11 186, 1996.

[31] J. Furthmüller G. Kresse. Efficiency of ab-initio total energy calculations for metals and semiconductors using a plane-wave basis set. *Physical Review*, 6:15–50, 1996.

[32] Joachim Sauer Pascal Raybaud Marius-Christian Silaghi, Céline Chizallet. Dealumination mechanisms of zeolites and extra-framework aluminum confinement. *Journal of Catalysis*, 339:242–255, 2016.

[33] Maxwell I.E. Biswas, J. Octane enhancement in fluid catalytic cracking. *Applied Catalysis*, 58:1–18, 1990.

List of Figures

List of Tables